

From the microstructure to diffusion MRI, and back

Denis S. Grebenkov

May 5, 2015

Contents

1	Introduction	2
2	Mathematical background	3
2.1	Bloch-Torrey equation	3
2.2	Boundary conditions	5
2.3	Diffusion-weighting magnetic field	6
2.4	Characteristic scales	12
2.5	Solutions of the Bloch-Torrey equation	14
3	Theoretical approaches	16
3.1	Narrow-pulse approximation	16
3.2	Gaussian phase approximation	20
3.2.1	Apparent diffusion coefficient	22
3.2.2	Short-time asymptotics	25
3.2.3	Long-time asymptotics: isolated pores	26
3.2.4	Long-time asymptotics: connected pores	27
3.3	Diffusion in multi-compartmental tissue	30
3.3.1	Multi-exponential and distributed signals	30
3.3.2	Bi-exponential model	32
3.3.3	Kärger model	33
3.3.4	Anomalous diffusion models	37
3.3.5	Effective medium theory	38
3.4	Towards microscopic geometric models	39
3.5	Towards high gradients	40
4	Conclusions and perspectives	45

1 Introduction

In this chapter, we discuss the mathematical background of diffusion magnetic resonance imaging (dMRI), also known as diffusion weighted imaging (DWI) and nuclear magnetic resonance (NMR) diffusometry. This non-invasive technique is broadly applied in material sciences to investigate structural and transport properties of porous media (such as sedimentary rocks, concrete, cement, gypsum, clays), as well as in medicine and neurosciences to study anatomical, physiological, and functional properties of biological tissues and organs such as brain, skin, lungs, bones [1–8]. Conventional MRI employs inhomogeneous magnetic fields to locally excite the nuclei (e.g., water protons) in a small region of a sample, and then to measure the resulting overall magnetization in this region (called a voxel). Repeating the procedure for many voxels yields an image of the sample, with typical spatial resolution from around 1 mm in clinical scanners to $\sim 50 \mu\text{m}$ in research scanners for small animals and mineral samples. This resolution is essentially limited by thermal motion of the nuclei which can diffuse away from their voxel during the measurement. Being unable to prevent diffusion, one attempts to benefit from it to gain new information on the microstructure at much smaller length scales. For this purpose, a diffusion-weighting (or diffusion-sensitizing) gradient is applied to create spatially uneven nuclear precession and thus encode random trajectories of the nuclei. When the nuclei diffuse inside a heterogeneous medium, the statistics of their random displacements is affected by the presence of walls or obstacles. Although these microscopic restrictions are not visible at the spatial resolution of MRI, their geometric features are statistically aggregated into the macroscopic signal. Roughly speaking, denser obstacles are more difficult to diffuse through, the nuclei are then less spread, their precessions are less dephased, and the macroscopic signal is thus less attenuated. Measuring the signal at different diffusion times and gradients, one aims at inferring the morphological structure of a sample and to characterize the dynamics of a system. In spite of numerous applications of dMRI and more than sixty years of intensive theoretical work, this formidable inverse problem has not been fully solved.

Starting from the Bloch-Torrey equation that provides the accurate microscopic description of the magnetization evolution, we overview various theoretical and phenomenological approaches to relate the microstructure to the macroscopic signal. Both classical approaches and more recent advances will be presented, with the main focus on the mathematical aspects. In spite of an attempt of a systematic presentation, the chapter is not exhaustive, while the choice of the presented materials is biased by the author's own research interests and views.

2 Mathematical background

2.1 Bloch-Torrey equation

In dMRI, the magnetic field is first applied to split the energy level of the diffusing nuclei and to create two distinct populations. The resulting magnetization is oriented along the magnetic field which is conventionally directed along the z axis: $\mathbf{B} = (0, 0, B_z)$. After that, the 90° radio-frequency (rf) magnetic field pulse flips the nuclear magnetization into the transverse plane (xy) where it starts to precess with the Larmor frequency γB_z , γ being the nuclear gyromagnetic ratio (in units rad/T/s). The magnetization $\mathbf{M} = (M_x, M_y, M_z)$ obeys the Bloch-Torrey equation [9]

$$\begin{aligned}\frac{\partial M_x}{\partial t} &= \nabla \cdot \mathbf{D} \nabla M_x + \gamma (\mathbf{M} \times \mathbf{B})_x - \frac{M_x}{T_2}, \\ \frac{\partial M_y}{\partial t} &= \nabla \cdot \mathbf{D} \nabla M_y + \gamma (\mathbf{M} \times \mathbf{B})_y - \frac{M_y}{T_2}, \\ \frac{\partial M_z}{\partial t} &= \nabla \cdot \mathbf{D} \nabla M_z + \gamma (\mathbf{M} \times \mathbf{B})_z - \frac{M_z - M_0}{T_1},\end{aligned}$$

where ∇ is the gradient operator, \cdot and \times denote the scalar and vector products, respectively. The right-hand side of this equation includes three different mechanisms affecting the magnetization: (i) diffusion of the nuclei with the diffusion tensor \mathbf{D} (in units m^2/s); (ii) precession around the magnetic field \mathbf{B} , and (iii) relaxation to the equilibrium magnetization $\mathbf{M}_{\text{eq}} = (0, 0, M_0)$. The longitudinal and transverse relaxation times T_1 and T_2 reflect two distinct relaxation mechanisms for the transverse and longitudinal components of the magnetization: the so-called spin-lattice relaxation (T_1) and the spin-spin relaxation (T_2). Combining M_x and M_y into the complex-valued transverse magnetization $m = M_x + iM_y$ and writing explicitly the components of the vector product $\mathbf{M} \times \mathbf{B}$ yield the conventional compact form of the Bloch-Torrey equation:

$$\frac{\partial m(\mathbf{r}, t)}{\partial t} = \left[\nabla \cdot \mathbf{D} \nabla - i\gamma B_z(\mathbf{r}, t) - \frac{1}{T_2} \right] m(\mathbf{r}, t). \quad (1)$$

The precessing magnetization of the nuclei induces electric current in the coils surrounding the bore of the magnet that allows one to monitor the evolution of the total magnetization in time. In other words, although the Bloch-Torrey equation provides the accurate microscopic description of the magnetization evolution, one can only measure the macroscopic signal from the voxel,

$$S = \int d\mathbf{r} m(\mathbf{r}, t), \quad (2)$$

the magnetization $m(\mathbf{r}, t)$ itself remaining inaccessible experimentally. Albeit this averaging eliminates structural information about the medium, the great challenge of dMRI consists in recovering some lost geometric features from understanding the effect of a medium onto diffusion and the resulting macroscopic signal.

Although the transverse relaxation of a nucleus can in general depend on its position \mathbf{r} , we assume the transverse relaxation time T_2 to be space-independent. In other words, all the nuclei are affected by the transverse relaxation in the same way, and the resulting signal attenuation is factored out as $\exp(-t/T_2)$, independently of diffusion and precession. The related term in the Bloch-Torrey equation (1) can be omitted. Similarly, the diffusion tensor \mathbf{D} is treated as space-independent. Moreover, we make a stronger assumption that diffusion of the nuclei at the *microscopic* level is isotropic so that the diffusion tensor is reduced to the diffusion coefficient D . We emphasize that this assumption does not prevent to observe anisotropic diffusion at the macroscopic level, e.g., for a bundle of neurons in brain dMRI [10]. In fact, our isotropic assumption ignores possible structural features of the medium on even smaller scales than those of the Bloch-Torrey equation (e.g., the fine structure of the cytoplasm is replaced by a homogeneous medium surrounded by a permeable membrane). Such coarse-grained simplifications are mandatory to describe multiscale complex systems such as biological tissues. At the same time, the applicability of these simplifications is not granted and has to be carefully thought of for each studied system. Although we will ignore microscopic anisotropy for the sake of simplicity, the majority of presented results can be extended to the anisotropic case. The two assumption simplify the Bloch-Torrey equation (1) as

$$\frac{\partial m(\mathbf{r}, t)}{\partial t} = D\nabla^2 m(\mathbf{r}, t) - i\gamma B_z(\mathbf{r}, t)m(\mathbf{r}, t), \quad (3)$$

where ∇^2 is the Laplace operator describing isotropic diffusion. This is a standard diffusion-reaction equation, except that the second (reactive) term contains the imaginary “reaction rate” $i\gamma B_z(\mathbf{r}, t)$. This “minor” detail completely changes many properties of this partial differential equation, e.g., the governing operator $D\nabla^2 - i\gamma B_z(\mathbf{r}, t)$ is in general not Hermitian (see Sec. 3.5).

It is instructive to evoke the probabilistic interpretation of the macroscopic signal [5]. Diffusing in inhomogeneous magnetic field $B_z(\mathbf{r}, t)$, each nucleus acquires a random phase φ_t obtained by integrating the position-dependent Larmor frequency $\gamma B_z(\mathbf{r}, t)$ along the random trajectory $\mathbf{R}(t)$ of

the nucleus:

$$\varphi_t = \int_0^t dt' \gamma B_z(\mathbf{R}(t'), t'). \quad (4)$$

This random variable is a functional of the random trajectory $\mathbf{R}(t)$. When there is no T_1/T_2 relaxation, the amplitude of the local magnetization does not change, and the macroscopic signal can be obtained by averaging the phase factors $e^{i\varphi_t}$ over all the nuclei. Since the number of nuclei in a macroscopic voxel is gigantic, the average can be replaced by the expectation over all random trajectories $\mathbf{R}(t)$:

$$S = S_0 \mathbb{E}\{e^{i\varphi_t}\}, \quad (5)$$

where the starting points of trajectories are uniformly distributed over the voxel, and S_0 is the reference signal without diffusion-weighting gradient. In other words, the macroscopic signal appears as the characteristic function of the phase φ_t in Eq. (4), while its relation to the integral (2) of the solution $m(\mathbf{r}, t)$ of the Bloch-Torrey equation (3) is known as the Feynman-Kac formula [5, 11–13].

2.2 Boundary conditions

Except for the trivial case of unrestricted diffusion in the whole space, the Bloch-Torrey equation (1) has to be completed by boundary conditions on every surface that may hinder the motion of the nuclei. Three boundary conditions are typically considered (Fig. 1):

- Neumann boundary condition for an inert impermeable surface that just reflects the nuclei and does not affect their magnetization:

$$\frac{\partial m(\mathbf{r}, t)}{\partial n} = 0, \quad (6)$$

where $\partial/\partial n = (\mathbf{n}_r \cdot \nabla)$ is the normal derivative oriented outwards the medium (i.e., the derivative is taken along the normal unit vector \mathbf{n}_r at the boundary point \mathbf{r}). This boundary condition is often employed to simplify the analysis when permeation or surface relaxation can be neglected.

- Robin boundary condition for a relaxing impermeable surface on which the nuclei can partly lose their magnetization:

$$D \frac{\partial m(\mathbf{r}, t)}{\partial n} + \rho m(\mathbf{r}, t) = 0, \quad (7)$$

where ρ is the surface relaxivity (in units m/s). This boundary condition is relevant for mineral samples whose solid walls contain magnetic impurities that relax the magnetization of the nuclei near the wall [14–16]. Note that Eq. (7) was also used to describe “one-way permeation” (or leakage) through a membrane [17–19], although this description remains oversimplified as the nuclei are not allowed to permeate back. One retrieves the Neumann boundary condition (6) by setting $\rho = 0$ (no surface relaxation).

- Transmission boundary condition for a permeable surface between two adjacent domains (e.g., intracellular and extracellular regions in a tissue [20]):

$$D_+ \frac{\partial m_+(\mathbf{r}, t)}{\partial n} = -D_- \frac{\partial m_-(\mathbf{r}, t)}{\partial n} = \kappa [m_-(\mathbf{r}, t) - m_+(\mathbf{r}, t)], \quad (8)$$

where $m_{\pm}(\mathbf{r}, t)$ denote the magnetization on two sides of the surface, D_{\pm} are the corresponding diffusion coefficients, and κ is the surface permeability (in units m/s) [21–23]. In contrast to former boundary conditions, Eq. (8) combines two conditions: the continuity of the magnetization flux across the surface (first relation) and the drop of magnetization due to a finite permeation (second relation). When $\kappa = 0$, there is no permeation across the surface, and one retrieves the Neumann boundary condition for both domains. In the limit $\kappa \rightarrow \infty$ (fully permeable surface), a finite magnetization flux is only possible by setting $m_-(\mathbf{r}, t) = m_+(\mathbf{r}, t)$, i.e., by imposing the continuity of the magnetization across the boundary. Finally, setting $m_-(\mathbf{r}, t) = 0$ in one domain, one recovers the Robin boundary condition (7) for the other domain.

We excluded from the above list the so-called Dirichlet boundary condition, $m(\mathbf{r}, t) = 0$, which is often imposed for diffusion-reaction processes. This condition describing a perfectly reactive surface which would immediately relax the magnetization of any coming nucleus, is not realistic for dMRI.

Since the solution $m(\mathbf{r}, t)$ of the Bloch-Torrey equation depends on boundary conditions, the microstructure of a medium is incorporated *implicitly* into the magnetization, resulting in an intricate relation between the microstructure and the macroscopic signal.

2.3 Diffusion-weighting magnetic field

Inferring the structural properties of a medium from the macroscopic signal S would be hopeless if there was no possibility to control the magnetic

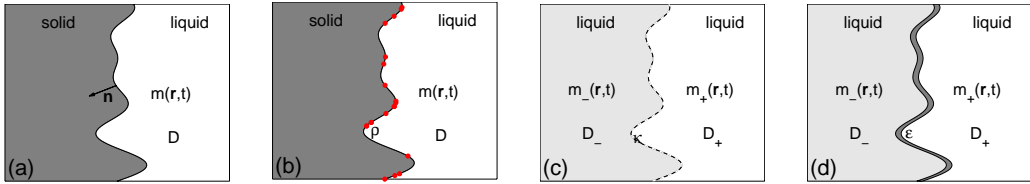


Figure 1: Illustration of several boundary conditions employed in dMRI: **(a)** inert impermeable solid/liquid interface reflects all nuclei yielding zero magnetization flux at the wall (Neumann boundary condition); **(b)** paramagnetic impurities (red circles) dispersed on the solid impermeable wall partly relax the magnetization at the wall and are modeled through surface relaxivity ρ (Robin boundary condition); **(c,d)** diffusive exchange between two compartments can be modeled either by infinitely thin semi-permeable membrane (dashed line) with the permeability κ in the transmission boundary condition on the magnetizations $m_{\pm}(\mathbf{r}, t)$ on both sides **(c)**, or by a thick membrane with a smaller diffusion coefficient D_m and continuity conditions on the magnetizations in three regions **(d)**. When the membrane thickness ϵ is small, the last situation can be approximated by the transmission boundary condition with $\kappa = D_m/\epsilon$.

field $B_z(\mathbf{r}, t)$. The choice and controlled variations of the magnetic field offer numerous ways to tackle with the inverse problem. In a standard dMRI measurement, $B_z(\mathbf{r}, t)$ includes two terms: a constant magnetic field B_0 to induce sufficient magnetization, and a small spatially inhomogeneous correction to encode the diffusive motion. The first term affects all the nuclei in the same way that allows one to factor out its contribution to the solution of the Bloch-Torrey equation as $e^{-i\gamma B_0 t}$. The second term is necessary to distinguish the precession of the nuclei in different spatial positions. The simplest and most common choice of the second term is a linear gradient in a prescribed direction, i.e. $B_z(\mathbf{r}, t) = B_0 + (\mathbf{r} \cdot \mathbf{g}(t))$. While the gradient $\mathbf{g}(t)$ can in general vary in amplitude and direction, most dMRI experiments are realized with a fixed gradient direction \mathbf{e} during one acquisition cycle. It is therefore convenient to factor out the dimensionless temporal profile $f(t)$ as

$$B_z(\mathbf{r}, t) = B_0 + g f(t) (\mathbf{e} \cdot \mathbf{r}). \quad (9)$$

The choice of the amplitude g (in units T/m), direction \mathbf{e} , and temporal profile $f(t)$ of the linear gradient remains at experimentalist's hands. There are several standard choices for the temporal profile (see Fig. 2).

(i) The simplest choice $f(t) = 1$ produces the signal known as free induction decay (FID). Although this choice is particularly simple from both the-

oretical and experimental points of view, it is not used for diffusion measurements because of the rephasing problem: small heterogeneities of a medium lead to uncontrollable dephasing of the nuclei and fast decay of the signal [1].

(ii) Hahn proposed to apply the 180° rf pulse at time Δ (in the middle of acquisition) in order to invert the precession direction of the nuclei [24]. The dephasing acquired during the first period (from 0 to Δ) is compensated by the rephasing during the second period (from Δ to 2Δ). At the so-called echo time $T = 2\Delta$, the nuclei are again in phase and form the macroscopic signal called an echo. The rephasing is complete for immobile nuclei and incomplete for diffusing nuclei, signal attenuation being related to diffusion. The effect of the rephasing 180° rf pulse is mathematically equivalent to inverting the gradient direction (Fig. 2a). The effective temporal profile is then

$$f(t) = \begin{cases} 1, & 0 < t < \Delta, \\ -1, & \Delta < t < 2\Delta. \end{cases} \quad (10)$$

(iii) Carr-Purcell-Meiboom-Gill sequence consists in a multiple repetition of 180° rf pulses to produce a train of echoes [25, 26]. The progressive attenuation of their amplitudes yields the effective attenuation rate which includes the T_2 relaxation, the diffusion effect onto incomplete rephasing, surface relaxation or other mechanisms.

(iv) Stejskal and Tanner proposed a pulsed-gradient sequence with two rectangular gradient pulses of duration δ separated by the inter-pulse time Δ (Fig. 2b) [27, 28]:

$$f(t) = \begin{cases} 1, & 0 < t < \delta, \\ -1, & \Delta < t < \Delta + \delta, \\ 0, & \text{otherwise} \end{cases} \quad (11)$$

The Hahn echo is retrieved by setting $\delta = \Delta$. The separation of the pulse duration δ and the inter-pulse delay Δ gave a new degree of freedom in the analysis of dMRI measurements. This Stejskal-Tanner sequence and its extensions (e.g., the trapeze-shaped gradient pulses shown in Fig. 2c whose form is closer to experimental setup) are the most often choice in dMRI. In experiment, both gradient pulses are usually slightly delayed from the respective 90° and 180° rf pulses.

Stimulated spin-echo sequences [2–4], in which the refocusing 180° rf pulse is replaced by two new 90° rf pulses, can be described by the temporal profile (11). The first of these 90° rf pulses turns the nuclei back to the longitudinal direction (z axis) in order to preserve the magnetization from the T_2 spin-spin

relaxation which is usually much faster than the T_1 spin-lattice relaxation. The last 90° rf pulse moves the stored nuclei again to the transverse plane for “decoding” by the second gradient pulse. This “trick” is used to overcome the T_2 relaxation mechanism and to allow for long-time measurements (up to seconds) but it does not alter the gradient encoding and all the consequent mathematical analysis. In other words, from the diffusion-weighting perspective, there is no difference between spin-echo and stimulated spin-echo sequences.

(v) More recently, rectangular gradient pulses of different amplitudes and durations were analyzed [29–31]:

$$f(t) = \begin{cases} 1, & 0 < t < \delta, \\ -\beta, & \Delta < t < \Delta + \delta/\beta, \\ 0, & \text{otherwise} \end{cases} \quad (12)$$

where β is a parameter of the sequence (Fig. 2d). We emphasize that the amplitude and duration of the second pulse are modified to still fulfill the so-called rephasing condition

$$\int_0^T dt f(t) = 0. \quad (13)$$

This condition is satisfied by all sequences that produce an echo.

(vi) Oscillating gradient profiles (Fig. 2e) were suggested to access the short-time scales of the diffusive motion [32–36].

It is worth emphasizing that the macroscopic signal is experimentally accessible only at the echo time T , in contrast to the mathematical description which accesses $m(\mathbf{r}, t)$ and thus S at any time t . Bearing in mind this experimental constraint, the analysis of the inverse problem should be restricted to a single value $S(T)$. At the same time, measurements can be repeated for different gradient amplitudes and directions, as well as for different temporal profiles (e.g., different Δ and/or δ). In spite of numerous proposed sequences, this opportunity is not yet fully explored.

As mentioned earlier, we restrict the analysis to the common situation when the gradient direction \mathbf{e} is fixed, while its amplitude varies in time. This restriction does not prevent one to repeat independent measurements in different gradient directions to access the macroscopic anisotropy of the sample. More generally, one can apply two or many pairs of gradient pulses successively to probe correlations between displacements in different directions [37–43]. This is an extension of CPMG sequence in which two gradient

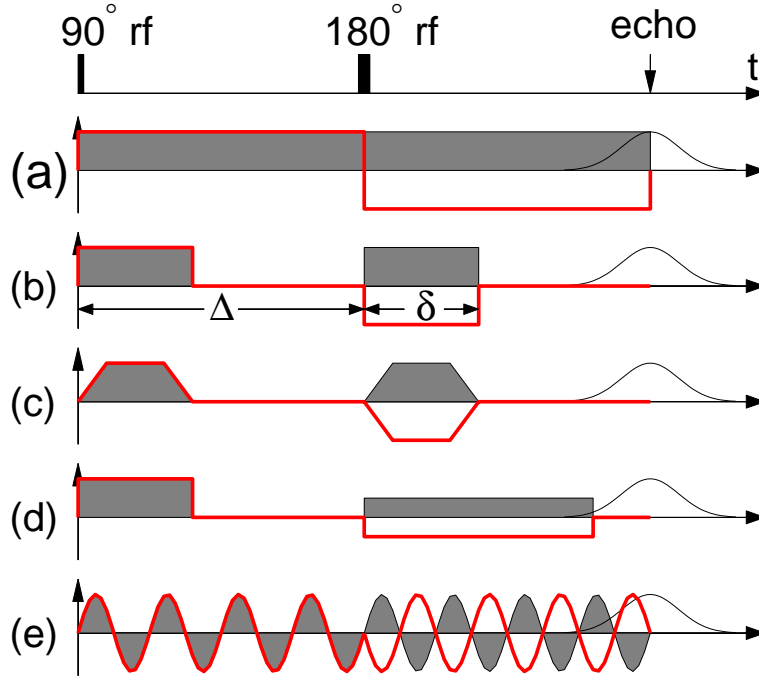


Figure 2: Several temporal profiles of the applied gradient: (a) Hahn echo, (b) bipolar rectangular (Stejskal-Tanner) profile, (c) trapeze-shaped profile, (d) rectangular profile with unequal pulses, and (e) oscillating sine profile. The thick red line indicates the effective temporal profile $f(t)$, in which the second gradient polarity is inverted by the 180° rf pulse. The echo emerges at $t = 2\Delta$, where Δ is the inter-pulse delay (between the exciting 90° and refocusing 180° rf pulses).

pulses in each pair are oppositely directed to ensure the refocusing condition, while gradient directions between pairs can be chosen arbitrarily. These so-called double-PGSE sequences were argued to be more sensitive in detecting local diffusion anisotropy than their single-PGSE counterpart but this issue remains controversial [44]. Although most results of the chapter can be extended to double-PGSE sequences, we do not discuss these points.

The above discussion concerned only the diffusion-weighting gradients. In both conventional and diffusion MRI, another kind of magnetic field gradients, the so-called imaging gradients, are used to excite the nuclei locally and thus to create the magnetization selectively in a well localized macroscopic region (voxel) of a sample. By means of imaging gradients, one can probe the diffusive motion and infer the geometric properties of a sample in various voxels. For instance, one can create a map of inferred properties

over the sample on larger scales than the size of a voxel (e.g., typical voxel size for human brain imaging is around 1 mm, while the field of view of the head can be 10-20 cm). In contrast, imaging gradients do not help to access to smaller scales, i.e., the microstructure of the medium. The imaging and diffusion-weighting gradients should not be confused. Throughout this chapter, we focus on the signal in a macroscopic region, either the whole sample, or one selected region (a voxel). In this way, we do not distinguish diffusion NMR or NMR diffusometry (when the signal comes from the whole sample) and diffusion MRI (when the signal comes from a macroscopic region of the sample). In both cases, the analysis of diffusion effects onto the macroscopic signal is essentially the same, while it is repeated for each voxel in the case of dMRI¹. In particular, we do not discuss imaging gradients any more.

Finally, the form (9) of the magnetic field ignores internal gradients that often exist in a heterogeneous sample. In particular, differences in the magnetic properties of liquid and solid phases create susceptibility-induced internal gradients near the liquid-solid interface. Although these local gradients rapidly decay from the interface, their contribution can be dominant in small pores (as compared to externally applied linear gradients) that may significantly bias diffusion measurements. In the simplest model, the parasitic effect of internal gradients can be incorporated through surface relaxation but this description is oversimplified as the direction of internal gradients is ignored. In order to check for internal gradients bias, diffusion-weighted measurements can be performed for two opposite directions of the applied gradient, i.e., with temporal profiles $f(t)$ and $-f(t)$. Two signals are identical without internal gradients, while their difference allows one to estimate internal gradients and to (partly) correct for their effect. Alternatively, internal gradients can potentially substitute externally applied diffusion-weighting gradients for encoding trajectories of the nuclei [47]. However, a reliable interpretation of such measurements is still challenging due to the unknown distribution of internal gradients over the sample and the consequent uncontrollable effect onto the macroscopic signal. We do not further discuss these effects.

¹We mention another, more technical difference between these two techniques. When the signal is acquired over a voxel, an appropriate boundary condition has to be imposed on the outer boundary of the voxel. This condition should account for the nuclei that were excited in the voxel and then moved to neighboring voxels so that they do not contribute to the macroscopic signal in the studied voxel. To account for the consequent loss of the signal, one often imposes the Robin boundary condition. Another choice consists in pseudo-periodic boundary conditions [45, 46]. Finally, one can consider a larger domain (including the neighboring voxels) and use non-uniform excitation and pick-up functions to delimit the current voxel [23]. Whatever the method is used, the effect of inter-voxel nuclei migration is typically small, at least for large voxels.

2.4 Characteristic scales

From now on, we focus on the following Bloch-Torrey equation

$$\frac{\partial m(\mathbf{r}, t)}{\partial t} = D\nabla^2 m(\mathbf{r}, t) - i\gamma g f(t)(\mathbf{e} \cdot \mathbf{r})m(\mathbf{r}, t), \quad (14)$$

subject to the uniform initial condition over the voxel of volume V : $m(\mathbf{r}, 0) = 1/V$, and eventual boundary conditions as discussed in Sec. 2.2. This equation includes two separate causes of the magnetization evolution: diffusion and dephasing. It is instructive to quantify the relative contributions of these two terms through characteristic length (or time) scales. The ratio between the dimensional coefficients in front of these terms, D and γg , has units of a volume that yields a natural gradient length ℓ_g :

$$\ell_g = (D/(\gamma g))^{1/3}. \quad (15)$$

Note that this length appears independently of the temporal profile and, in particular, of the echo time. Large values of ℓ_g mean diffusion dominating contribution. But large with respect to what? What are the other length scales of the problem? The introduction of other length scales is less straightforward.

The nuclei undergoing *unrestricted* diffusion in the whole space travel on average the distance $\sqrt{6DT}$ during the experiment of duration T . However, this distance is not representative in general by several reasons: (i) obstacles, solid walls, tortuous channels or pores hinder the diffusive motion and may either slow down or even alter normal diffusion; it may therefore be unjustified to use the intrinsic diffusion coefficient D , especially for long measurements; (ii) since dMRI probes diffusion in the gradient direction, displacements in other directions are less relevant; the factor 6 (coming from the three-dimensional character of diffusion) may need to be replaced by factor 2. As a consequence, the expression $\sqrt{6DT}$ can only estimate orders of magnitude of the diffusion length. For this reason, we remove the uncertain factor 6 from this expression and call the diffusion length $\ell_D = \sqrt{DT}$, bearing in mind that it is only a rough estimate.

Another often employed length scale is the dephasing length $\ell_d = 1/(\gamma g T)$ which characterizes the overall phase shift during time T . Once again, this notion is ambiguous because the gradient causing the dephasing is not necessarily switched on during the whole measurement. On the contrary, short gradients pulses are often applied, in which case the above quantity may be misleading. For the Stejskal-Tanner sequence, it is more appropriate to define the dephasing length as the inverse of the wavevector amplitude $q = \gamma g \delta$:

$\ell_q = 1/q = 1/(\gamma g \delta) = (T/\delta)\ell_d$. Whatever the definition is used, the dephasing length strongly depends on the temporal profile. Note that the gradient length, diffusion length, and dephasing length are not independent, and one can be expressed through the two others, e.g., $\ell_d = \ell_g^3/\ell_D^2$.

While the above length scales characterize the experimental setup and the intrinsic motion of the nuclei, the microstructure can impose a set of geometric length scales. In the simplest situation, one deals with monodisperse obstacles of a single size L . In Sec. 3.2.3, we will discuss restricted diffusion inside simple isolated pores (such as spheres or cylinders) which are characterized by their sizes. In turn, most mineral and biological samples exhibit polydispersity and are characterized by multiple length scales. One of the theoretical challenges in dMRI consists in developing appropriate statistical tools to aggregate multiple length scales of the sample into the macroscopic signal. In particular, several works aimed at determining the pore size distribution from the signal (see Sec. 3.3).

Finally, surface relaxation or permeation can be characterized by a length $\ell_\rho = D/\rho$ or $\ell_\kappa = D/\kappa$, respectively. This length can be interpreted as an effective distance traveled by the nucleus between the first arrival onto the surface and the full relaxation or permeation [48–50]. The role of the relaxation/permeation length in diffusion-reaction processes has been thoroughly investigated [5, 51–61].

Before starting any experiment or numerical simulation, it is instructive to estimate the characteristic length scales in order to anticipate the behavior of the macroscopic signal. For this purpose, we summarize the parameters and discuss the resulting length scales. For water diffusion, the proton gyromagnetic ratio is $\gamma \simeq 2.675 \cdot 10^8$ rad/T/s. The water diffusion coefficient D changes between $3 \cdot 10^{-9}$ m²/s at 37° (body temperature) and $2.3 \cdot 10^{-9}$ m²/s at 20° (room temperature), these variations being insignificant for estimating length scales. The gradient g varies from 0 to 30 – 50 mT/m in clinical scanners, to few T/m in small bore research scanners, and up to few hundreds of T/m in stray field experiments [62]. The gradient pulse duration δ can take values from 1 ms to tens or even hundreds of milliseconds. It is possible to get sub-millisecond values of δ but the non-rectangular form of the temporal profile has to be accounted for. The inter-pulse time $\Delta \geq \delta$ can be increased up to few hundreds of milliseconds or even seconds by using stimulating spin-echo sequences (Sect. 2.3). The water permeability can vary significantly among biological tissues, from 10^{-8} m/s for *Fundulus eggs* up to $(5 - 8) \cdot 10^{-5}$ m/s for red blood cells, brain and lung tissues (see [63–66] for summaries of permeabilities in different cells). Similarly, the surface relaxivity ρ varies from negligible values in some biological tissues up to $1.5 \cdot 10^{-5}$ m/s in limestone and $3 \cdot 10^{-5}$ m/s in sandstone [67, 68] (see also [69]). Combining

	Expression	min (μm)	max (μm)	parameter variations
ℓ_g	$(D/(\gamma g))^{1/3}$	~ 2	∞	g from 1 T/m to 0
ℓ_D	\sqrt{DT}	~ 2	~ 20	T from 1 ms to 100 ms
ℓ_q	$1/(\gamma g \delta)$	~ 0.5	∞	g from 1 T/m to 0, $\delta = 10$ ms
ℓ_ρ	D/ρ	~ 70	∞	ρ from $3 \cdot 10^{-5}$ m/s to 0
ℓ_κ	D/κ	~ 25	∞	κ from $8 \cdot 10^{-5}$ m/s to 0

Table 1: Characteristic length scales.

these parameters, one can estimate the characteristic length scales (Table 1) that are to be compared to the geometric length scales of a sample.

2.5 Solutions of the Bloch-Torrey equation

In spite of a simple form of the Bloch-Torrey equation, its solution is surprisingly complicated. An exact explicit solution of the Bloch-Torrey equation (14) is only available for unrestricted diffusion in the whole space [1, 70] for which the macroscopic signal takes the classical exponential form:

$$S = S_0 \exp(-Db), \quad (16)$$

where S_0 is the reference signal (without diffusion-weighting gradient), and the b -value is defined as [71]

$$b = \gamma^2 g^2 \int_0^T dt \left(\int_0^t dt' f(t') \right)^2, \quad (17)$$

where the rephasing condition (13) was assumed. For instance, the b -value for the Stejskal-Tanner profile reads as

$$b = \gamma^2 g^2 \delta^2 (\Delta - \delta/3). \quad (18)$$

Varying the magnetic field parameters (g , δ or Δ), one can access the diffusion coefficient D of freely diffusing molecules [72, 73]. For this sequence, $\Delta - \delta/3$ from Eq. (18) is often called the diffusion time.

The presence of any boundary with any (nontrivial) boundary condition violates the above solution. Even for the simplest confining domains such as cylinders or spheres, there is no exact explicit solution of the Bloch-Torrey equation with a nontrivial temporal profile $f(t)$. Few exact solutions are known only for one-dimensional configurations (e.g., semi-axis, interval, array of intervals) and involve infinite series of complex-valued Airy functions

[74, 75] (see Sec. 3.5). The very limited set of known analytical solutions illustrates the mathematical difficulties in understanding the interplay between the microstructure and the macroscopic signals. Missing the exact solutions of the problem stimulated numerous works on both numerical tools and approximations. The overwhelming majority of theoretical publications on dMRI deal with approximate solutions of the Bloch-Torrey equation that we discuss in the next section. To conclude this section, we mention three classes of numerical schemes employed to solve the Bloch-Torrey equation.

- **Monte Carlo simulations.** The probabilistic interpretation of the macroscopic signal as the characteristic function of the random phase suggests the most natural way for its computation. In fact, it is sufficient to simulate a random trajectory $\mathbf{R}(t)$ of the nucleus diffusing in a medium and then to compute the acquired phase φ_t in Eq. (4). Repeating this computation N times, one can approximate the macroscopic signal in Eq. (5) by the empirical average over N independent realizations of the random variable φ_t . This Monte Carlo method is very flexible and easy to implement for various microstructures [76–82]. Its major drawback is the slow convergence of the empirical average to the expectation (which typically goes as $1/\sqrt{N}$).
- **Finite differences method (FDM) and finite elements method (FEM).** The Laplace operator ∇^2 can be discretized on a regular lattice (finite differences) or an adaptive mesh (finite elements) that reduces the Bloch-Torrey PDE to a large system of linear ordinary differential equations [45, 46, 83–86]. This system can be solved numerically by an appropriate time discretization. Both finite difference and finite elements methods are usually more accurate than Monte Carlo simulations and can provide not only the macroscopic signal but also the magnetization $m(\mathbf{r}, t)$. In turn, the spatial discretization of complex multiscale media may lead to extremely large systems of equations, especially in three dimensions, that would prohibit their numerical solution (for comparison, the efficiency of Monte Carlo simulations is almost independent of the space dimension).
- **Matrix formalisms.** Considering the magnetic field $B_z(\mathbf{r}, t)$ in Eq. (14) as a perturbation of the Laplace operator, one can decompose the magnetization $m(\mathbf{r}, t)$ on the complete basis of Laplacian eigenfunctions when dealing with restricted diffusion in bounded domains [5, 87–91]. The projection onto eigenfunctions reduces the Bloch-Torrey PDE to an infinite system of linear differential equations which can be truncated and then solved numerically. The solution is obtained

by matrix operations which are fast and very accurate. Solving the Bloch-Torrey equation is thus “reduced” to computing Laplacian eigenfunctions. In general, this new problem is even more time-consuming than the original one. However, for a special class of “symmetric” domains, the Laplacian eigenfunctions are known explicitly [92] that tremendously speeds up computations and greatly improves the accuracy. Examples of such domains are intervals/rectangles/rectangular parallelepipeds, equilateral triangles, disks/cylinders, spheres, circular annuli and spherical shells, and multilayered structures [23, 29, 88, 89]. For these domains, the matrix formalisms are much faster and more accurate than other numerical techniques. Note that in earlier versions of matrix formalisms, the temporal profile was approximated by a finite sum of delta-functions [93–95].

Both Monte Carlo and finite differences/elements methods become more time-consuming at longer echo times T and higher gradients g . Evidently, longer T requires simulating longer trajectories or solving the system of linear equations for a larger number of time steps. In turn, higher gradients need finer time or space resolution for both techniques. For matrix formalisms, longer times do not present any problem, while higher gradients require larger matrices and thus may slow down computations.

3 Theoretical approaches

In the previous section, we presented the mathematical background to relate the macroscopic signal to the microstructure. We stressed that the microstructure appears implicitly through the boundary conditions to the Bloch-Torrey equation. How can one infer the microstructure without having an exact explicit solution of this equation? In this section, we discuss several theoretical approaches that were developed to overcome this problem. In particular, we present two classical approximations that are useful in many practically relevant cases: the narrow-pulse approximation (NPA) and the Gaussian phase approximation (GPA).

3.1 Narrow-pulse approximation

Since the Bloch-Torrey equation does not admit simple solutions for generic temporal profiles $f(t)$, is it possible to simplify the related mathematics by adapting the physical setup? After all, the magnetic field is the “ingredient” of the problem that is under an experimentalist’s control. Stejskal and Tanner

gave an elegant solution by suggesting to narrow the gradient pulses [27, 28]. When the pulse duration δ is very short, the contribution of the diffusion term in the Bloch-Torrey equation (14) can be neglected as compared to that of the gradient term. Solving this equation without the diffusion term for $f(t) = 1$ during $0 < t < \delta$ yields $m(\mathbf{r}, \delta) = e^{-i\gamma\delta(\mathbf{g}\cdot\mathbf{r})}/V$, where the factor $1/V$ comes from the initial condition. When the gradient pulse is switched off, the Bloch-Torrey equation becomes simply the diffusion (or heat) equation which is easier to solve and analyze [96, 97]. A general solution of the diffusion equation can be expressed through the diffusion propagator, $G_t(\mathbf{r}_0, \mathbf{r})$, which satisfies

$$\frac{\partial G_t(\mathbf{r}_0, \mathbf{r})}{\partial t} = D\nabla^2 G_t(\mathbf{r}_0, \mathbf{r}), \quad (19)$$

subject to the initial condition $G_0(\mathbf{r}_0, \mathbf{r}) = \delta(\mathbf{r}_0 - \mathbf{r})$ and eventual boundary conditions discussed in Sec. 2.2. The diffusion propagator characterizes the probability density of moving from \mathbf{r}_0 to \mathbf{r} in time t . Using the propagator and considering $m(\mathbf{r}, \delta)$ as a new initial condition, one gets

$$m(\mathbf{r}', t) = \frac{1}{V} \int_{\Omega} d\mathbf{r} e^{-i\gamma\delta(\mathbf{g}\cdot\mathbf{r})} G_{t-\delta}(\mathbf{r}, \mathbf{r}') \quad (\delta < t < \Delta).$$

Applying the same arguments for the second gradient pulse and the remaining gradient-free period, one gets the macroscopic signal at the echo time 2Δ as

$$S = \frac{1}{V} \int_{\Omega} d\mathbf{r} \int_{\Omega} d\mathbf{r}' \int_{\Omega} d\mathbf{r}'' e^{-i\gamma\delta(\mathbf{g}\cdot\mathbf{r})} G_{\Delta-\delta}(\mathbf{r}, \mathbf{r}') e^{i\gamma\delta(\mathbf{g}\cdot\mathbf{r}')} G_{\Delta-\delta}(\mathbf{r}', \mathbf{r}''). \quad (20)$$

When there is no surface relaxation, the total magnetization is preserved, and the integral of $G_t(\mathbf{r}', \mathbf{r}'')$ over \mathbf{r}'' is equal to 1, from which

$$S = \frac{1}{V} \int_{\Omega} d\mathbf{r} \int_{\Omega} d\mathbf{r}' e^{-i\gamma\delta(\mathbf{g}\cdot(\mathbf{r}-\mathbf{r}'))} G_{\Delta}(\mathbf{r}, \mathbf{r}'), \quad (21)$$

where $\Delta - \delta$ was replaced by Δ in agreement with the assumption of very small δ . Changing the integration variable $\mathbf{R} = \mathbf{r} - \mathbf{r}'$, the macroscopic signal can be represented as a Fourier transform

$$S(\mathbf{q}) = \int_{\mathbb{R}^3} d\mathbf{R} e^{-i(\mathbf{q}\cdot\mathbf{R})} P(\mathbf{R}, \Delta), \quad (22)$$

where $\mathbf{q} = \gamma\delta\mathbf{g}$ is the wavevector² associated to the gradient \mathbf{g} , and

$$P(\mathbf{R}, \Delta) = \frac{1}{V} \int_{\Omega} d\mathbf{r} G_{\Delta}(\mathbf{r}, \mathbf{r} + \mathbf{R}) \quad (23)$$

²Here we omit the conventional prefactors 2π and $(2\pi)^{-1}$ in the Fourier transform and the definition of the wavevector.

is the averaged propagator (here we used the convention that $G_{\Delta}(\mathbf{r}, \mathbf{r}+\mathbf{R}) = 0$ if $\mathbf{r}+\mathbf{R} \notin \Omega$). Measuring the macroscopic signal at various \mathbf{q} and then inverting the Fourier transform, one can access to the averaged propagator that incorporates the geometric features of the microstructure. In other words, the particular choice of very narrow gradient pulses allows one to reduce the sophisticated NMR-dependent quantity, S , to a simpler purely diffusive characteristics of a medium, $P(\mathbf{R}, \Delta)$. This is a rare situation when the measurement features (gradients) can be fully disentangled from the geometric characteristics.

For simple isolated domains (e.g., slab, cylinder, sphere), the diffusion propagator is known explicitly from which the averaged propagator and the macroscopic signal can be deduced [78, 98–100]. For instance, the NPA signal for an isolated slab of width L and for an isolated sphere of radius L are respectively

$$S = 2(qL)^2 \left(\frac{1 - \cos(qL)}{(qL)^4} + 2 \sum_{n=1}^{\infty} e^{-D\pi^2 n^2 \Delta / L^2} \frac{1 - (-1)^n \cos(qL)}{(\pi^2 n^2 - (qL)^2)^2} \right), \quad (24)$$

and

$$S = 6(qL)^2 \sum_{n,k=0}^{\infty} e^{-D\lambda_{nk} \Delta / L^2} \frac{(2n+1)\lambda_{nk}}{\lambda_{nk} - n(n+1)} \frac{[j'_n(qL)]^2}{[\lambda_{nk} - (qL)^2]^2}, \quad (25)$$

where $j'_n(z)$ is the derivative of the spherical Bessel function $j_n(z)$ of the first kind, and $\sqrt{\lambda_{nk}}$ are the positive roots of the equation $j'_n(z) = 0$ ($n = 0, 1, 2, \dots$), enumerated by an index $k = 0, 1, 2, \dots$. Note that $\lambda_{0,0} = 0$, and the ratio $\lambda_{nk}/(\lambda_{nk} - n(n+1))$ is set to $3/2$ for $n = k = 0$.

At long times Δ , the NPA signal exhibits oscillating behavior known as diffusion-diffraction patterns [98, 99]. This is particularly clear in the limit $\Delta \rightarrow \infty$, when all terms except the one with $n = k = 0$ vanish, and the signals in Eqs. (24, 25) approach to

$$S_{\Delta=\infty} = \begin{cases} \frac{2(1 - \cos(qL))}{(qL)^2} & \text{(slab),} \\ \frac{9[qL \cos(qL) - \sin(qL)]^2}{(qL)^6} & \text{(sphere).} \end{cases} \quad (26)$$

Both functions oscillate and have infinitely many zeros, e.g., the zeros for a slab are at $qL = 2\pi, 4\pi, 6\pi, \dots$, while the first zero for a sphere is at $qL \approx 4.4934$. Detecting the first minimum of the NPA signal at long times allows one to estimate the size L of the confining domain.

Figure 3 illustrates the oscillating character of the signal for water molecules diffusing in isolated slab and sphere. The macroscopic signal S for a Stejskal-Tanner rectangular profile is computed by the matrix formalism [23, 89]. The

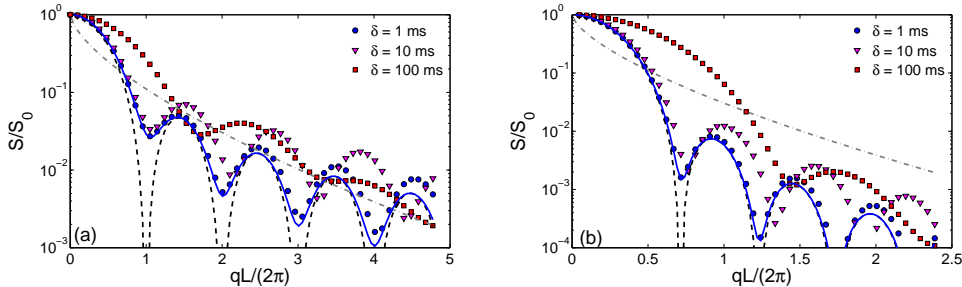


Figure 3: Signal attenuation S/S_0 as a function of $qL/(2\pi) = \gamma g \delta L/(2\pi)$ for diffusion in a slab of width $L = 30 \mu\text{m}$ **(a)** and in a sphere of radius $L = 15 \mu\text{m}$ **(b)**, with $D = 2.3 \cdot 10^{-9} \text{ m}^2/\text{s}$, $\Delta = 100 \text{ ms}$, and three values of the gradient pulse duration: $\delta = 1, 10, 100 \text{ ms}$. In order to keep the same range of q for three curves (with $q_{\text{max}} = 1 \mu\text{m}^{-1}$), the gradient g was rescaled by 1, 1/10, and 1/100, respectively. Symbols present the signals computed by the matrix formalism (with very high accuracy). The solid line shows the NPA signal from Eqs. (24, 25), while the dashed line shows its asymptotic limit (26). The dash-dotted line indicates the asymptotic behavior (66) in the localization regime (see Sec. 3.5).

signal attenuation S/S_0 as a function of $qL/(2\pi)$ is shown by symbols for three gradient pulse durations: $\delta = 1, 10, 100 \text{ ms}$ (with $\Delta = 100 \text{ ms}$ for all cases). The NPA signal from Eqs. (24, 25) which formally corresponds to the limit $\delta \rightarrow 0$ and $g \rightarrow \infty$, is shown by solid line. One can see that the NPA signal accurately approximates the macroscopic signal at short gradient pulses ($\delta = 1 \text{ ms}$, circles), while this approximation gets worse at longer gradient pulses, as expected. Note that even at $\delta = 1 \text{ ms}$, the approximation starts to deviate after the third minimum. We also show the long-time limit (26) by dashed line. Experimental validation of the NPA approximation in simple domains was reported in [78]. The influence of surface relaxation onto the NPA signal was thoroughly investigated [78, 100].

The oscillating behavior of the macroscopic signal at long times is expected for any *bounded* domain Ω . In fact, in the long time limit (when $D\Delta \gg L^2$, L being the size of the domain), the starting and arrival points of the propagator $G_\Delta(\mathbf{r}, \mathbf{r}')$ in Eq. (21) become independent, $G_\Delta(\mathbf{r}, \mathbf{r}') \simeq 1/V$, and the macroscopic signal approaches the squared absolute value of the form-factor of the domain:

$$S_{\Delta=\infty} = \left| \frac{1}{V} \int_{\Omega} d\mathbf{r} e^{-i\gamma\delta(\mathbf{g}\cdot\mathbf{r})} \right|^2. \quad (27)$$

The location of the first minimum of this function determines the characteristic length scale of the domain. For instance, Callaghan and co-workers have applied this technique to investigate water diffusion in a disordered medium of monodisperse glass beads and to experimentally determine the average distance between neighboring beads [98].

It is worth noting that the signal in Eq. (27) appears here “almost” as the squared Fourier transform of the indicator function of the domain. While the amplitude the form-factor is available, its phase remains inaccessible because of identical gradient pulses. Recently, pulsed-gradient sequences with different pulses have been employed to overcome this limitation and to reconstruct the shape of simple confining pores from dMRI [29–31].

In spite of conceptual simplicity and numerous applications of the NPA, there are several drawbacks. (i) The assumption of immobile nuclei during the gradient pulse may not be valid, especially for gas diffusion. (ii) An experimental implementation of very short *and* strong gradient pulses (for getting appropriate wavevectors $q = \gamma g \delta$) has instrumental limitations. (iii) The analysis of diffusion-diffraction patterns becomes challenging for disordered media for which oscillations at various length scales superimpose, interfere, and may cancel each other. The seminal work by Callaghan *et al.* [98] on diffusion in monodisperse spherical beads remains one of the best experimental realizations of this technique in porous media. (iv) Finally, encoding just the starting and the arrival positions of the nuclei was suggested to simplify the analysis of dMRI measurements. This idea which was revolutionary in the sixties, has to be revised nowadays. In fact, encoding the whole trajectory of the nuclei can provide more substantial information on diffusion and microstructure, if appropriate “decoding” tools are developed.

3.2 Gaussian phase approximation

The Gaussian phase approximation (GPA) is another pillar of the modern dMRI. A naive argument behind the GPA consists in saying that diffusion in a medium would remain Gaussian but be slowed down due to bumping and rebounding of the nuclei on obstacles or walls. Under this hypothesis, one can still apply the exponential form (16) in which the intrinsic diffusion coefficient D is replaced by an effective or apparent diffusion coefficient (ADC) [101]:

$$S \simeq \exp(-\text{ADC } b), \quad (28)$$

with the b -value defined in Eq. (17). Measuring the macroscopic signal at several b -values allows one to estimate ADC which is related to the microstructure: tighter confinement is expected to yield smaller ADC. The

concept of ADC and the underlying GPA have found numerous applications, especially for medical imaging. For instance, ADC maps of brain and lungs were used to identify tumors and emphysematous regions, respectively [6–8, 102–106].

The success of the ADC concept is inherently based on the rigorous perturbative analysis of the macroscopic signal at weak gradients. The Taylor expansion of the exponential function in Eq. (5) at $t = T$ reads

$$\frac{S}{S_0} = 1 + i\mathbb{E}\{\varphi_T\} - \frac{1}{2}\mathbb{E}\{\varphi_T^2\} - \frac{i}{6}\mathbb{E}\{\varphi_T^3\} + \frac{1}{24}\mathbb{E}\{\varphi_T^4\} + \dots, \quad (29)$$

which, by using the properties of the exponential function, can also be written as the cumulant expansion:

$$\ln(S/S_0) = i\langle\varphi_T\rangle_c - \frac{1}{2}\langle\varphi_T^2\rangle_c - \frac{i}{6}\langle\varphi_T^3\rangle_c + \frac{1}{24}\langle\varphi_T^4\rangle_c + \dots, \quad (30)$$

where the cumulant moments $\langle\varphi_T^n\rangle_c$ can be expressed in terms of ordinary moments $\mathbb{E}\{\varphi_T^n\}$. The even-order moments determine the real part of the signal, while the odd-order terms set the imaginary part. Under the rephasing condition (13), all odd-order moments vanish, and the leading (lowest-order) contribution is given by the second moment $\langle\varphi_T^2\rangle_c = \mathbb{E}\{\varphi_T^2\}$. The Gaussian phase approximation consists in neglecting higher-order terms which are expected to be small at weak gradients (given that φ_T is proportional to the gradient g), from which

$$S \simeq S_0 \exp(-\mathbb{E}\{\varphi_T^2/2\}). \quad (31)$$

According to the definition (4), the second moment can be written in terms of the position autocorrelation function (PAF):

$$\mathbb{E}\{\varphi_T^2/2\} = \gamma^2 g^2 \int_0^T dt_1 f(t_1) \int_{t_1}^T dt_2 f(t_2) \mathbb{E}\{(\mathbf{R}(t_1) \cdot \mathbf{e})(\mathbf{R}(t_2) \cdot \mathbf{e})\}, \quad (32)$$

where we used the symmetry of PAF to order time variables t_1 and t_2 . For unrestricted diffusion, the PAF is well known, $\mathbb{E}\{(\mathbf{R}(t_1) \cdot \mathbf{e})(\mathbf{R}(t_2) \cdot \mathbf{e})\} = 2D \min\{t_1, t_2\}$, from which the second moment becomes precisely bD , and one retrieves Eq. (16), with the b -value from Eq. (17). Moreover, all higher-order cumulant moments of the *Gaussian* variable φ_T vanish, and Eq. (31) becomes exact.

3.2.1 Apparent diffusion coefficient

In the presence of obstacles, the random phase φ_T is not necessarily a Gaussian variable, but Eq. (31) is approximately valid for small gradients. The comparison of Eqs. (28, 31) yields the rigorous definition of the ADC:

$$\text{ADC}_0 \equiv \frac{\mathbb{E}\{\varphi_T^2/2\}}{b} = \frac{\prec \mathbb{E}\{(\mathbf{R}(t_1) \cdot \mathbf{e})(\mathbf{R}(t_2) \cdot \mathbf{e})\} \succ}{\prec 2t_1 \succ}, \quad (33)$$

where we introduced the “temporal average” $\prec F(t_1, t_2) \succ$ of any function $F(t_1, t_2)$ based on the temporal profile $f(t)$:

$$\prec F(t_1, t_2) \succ \equiv \int_0^T dt_1 f(t_1) \int_{t_1}^T dt_2 F(t_1, t_2). \quad (34)$$

The subscript 0 highlights that ADC_0 reflects the behavior of the signal at small gradients, as discussed below. As expected, one retrieves $\text{ADC}_0 = D$ for unrestricted diffusion. For very narrow gradient pulses ($\delta \rightarrow 0$), the ADC is related to the mean-square displacement of the nuclei along the gradient direction \mathbf{e} :

$$\text{ADC}_0 = \frac{\mathbb{E}\{([\mathbf{R}(\Delta) - \mathbf{R}(0)] \cdot \mathbf{e})^2\}}{2\Delta} \quad (\delta \rightarrow 0). \quad (35)$$

In this case, ADC_0 represents a purely geometric characteristic of the medium. In general, the ADC also incorporates the NMR features through the temporal profile $f(t)$.

While the GPA in Eq. (31) may or may not be valid, the definition (33) of ADC_0 is rigorous and always applicable. According to Eqs. (29, 30), the second moment and therefore ADC_0 can also be expressed through the signal as

$$\text{ADC}_0 = -\lim_{b \rightarrow 0} \frac{\partial(S/S_0)}{\partial b} = -\lim_{b \rightarrow 0} \frac{\partial \ln(S/S_0)}{\partial b}. \quad (36)$$

We emphasize that ADC_0 in Eq. (33) or (36) depends on the gradient direction \mathbf{e} and temporal profile $f(t)$, but it is independent of the gradient amplitude g . In particular, one often accesses the behavior of ADC_0 (which is also called time-dependent diffusion coefficient) as a function of the inter-pulse time Δ [89, 107–119]. The relation of ADC_0 to the second moment of the phase φ_T and thus to the PAF significantly simplifies theoretical analysis. As we briefly discuss below, many theoretical results have been obtained under the GPA. The mathematical problem is reduced from the Bloch-Torrey equation (including the gradient encoding) to computing the PAF for a diffusive process.

Before proceeding, several comments are in order (see also [120]).

(i) The definition of the ADC_0 in Eq. (33) from the second moment of the phase is different from the conventional definition, in which the ADC is either as the slope of a linear fit of $\ln(S/S_0)$ over a range of small b -values, or simply $-\ln(S(b)/S_0)/b$ at a single b -value [101]. When b -values are small, the conventional ADC is very close to ADC_0 from Eq. (33) or (36). In fact, the ADC_0 is an extrapolation of the conventional ADC to $b = 0$. So what is the difference between ADC and ADC_0 ? From theoretical point of view, the conventional definition remains inaccurate because the value of ADC depends on the used b -values. In other words, the conventional ADC may depend on gradient amplitude. Note that writing $\text{ADC} = -\ln(S/S_0)/b$ does not simplify the problem but just transforms one sophisticated object (the signal) into another sophisticated object (ADC). The major advantage of ADC_0 is that this quantity does not depend on the gradient amplitude (or b -value). From practical point of view, the interpretation of ADC as a characteristics of a medium is meaningful only when this characteristics does not depend on the way how it is measured. For instance, the use of ADC as a pathology biomarker requires that the measured ADCs in biological tissues of two individuals under similar physiological conditions are close to each other. However, ADC measurements realized by different groups (with different experimental scanners or protocols) are difficult to compare when ADC depends on the gradient. In medical practice, the measurement is often reduced to the reference signal S_0 and one diffusion-attenuated signal $S(b)$, from which the ADC is deduced. Such oversimplified measurements, in which the validity of the GPA is presumed without verification, have to be avoided. In many experimentally relevant cases, the GPA becomes invalid even at moderate b -values, and the extracted ADC significantly depends on the particular choice of the used b -values. It is therefore recommended to use ADC_0 instead of ADC. The value ADC_0 can be extrapolated from the measured signal by fitting $\ln(S/S_0)$ as an appropriate polynomial of b over the experimentally available range of b -values. This is a standard way to overcome instabilities and uncertainties which would emerge due to experimental noise if one tried to measure the signal at very small b -values.

(ii) When the gradient increases, the lowest order term $\mathbb{E}\{\varphi_T^2\}$ grows slower than the higher-order terms and progressively loses its leading role. When $\ln(S/S_0)$ as a function of b starts to deviate from a straight line, one can include the next-order term,

$$S \simeq S_0 \exp \left(-\frac{1}{2} \langle \varphi_T^2 \rangle_c + \frac{1}{24} \langle \varphi_T^4 \rangle_c \right), \quad (37)$$

where $\langle \varphi_T^2 \rangle_c = \mathbb{E}\{\varphi_T^2\}$ and $\langle \varphi_T^4 \rangle_c = \mathbb{E}\{\varphi_T^4\} - 3(\mathbb{E}\{\varphi_T^2\})^2$ under the rephasing

condition (while all odd moments vanish). The above relation is known as the kurtosis model:

$$S \simeq S_0 \exp \left(-\text{ADC}_0 b + \frac{1}{6} \text{ADK}_0 (\text{ADC}_0 b)^2 \right), \quad (38)$$

where

$$\text{ADK}_0 = \frac{\langle \varphi_T^4 \rangle_c}{(\langle \varphi_T^2 \rangle_c)^2} = \frac{\mathbb{E}\{\varphi_T^4\}}{(\mathbb{E}\{\varphi_T^2\})^2} - 3 \quad (39)$$

is the apparent diffusion kurtosis. This quantity characterizes how the phase distribution is far from the Gaussian one (for which $\text{ADK}_0 = 0$). Since diffusion is influenced by obstacles or walls, the ADK was empirically suggested an indicator of tissue heterogeneity, in addition to ADC_0 [121, 122]. In experiment, the ADK_0 can be obtained by fitting $\ln(S/S_0)$ by a polynomial of b . In theory, the fourth-order moment $\mathbb{E}\{\varphi_T^4\}$ and the consequent ADK_0 can be expressed through the four-point correlation function [5], but these expressions are cumbersome and of little practical use. Although the kurtosis model allows one to fit the macroscopic signal over a slightly wider range of b -values, the unphysical growth of Eq. (38) with b leads to a complete failure of this model at larger b -values.

(iii) The inclusion of the sixth- and higher-order moments is of little interest. From practical point of view, it is difficult to accurately fit these terms which become perceptible only at higher b -values at which the signal may already be attenuated and thus strongly affected by noise. From theoretical point of view, the computation of these terms from multiple correlation functions becomes practically unfeasible [123] (even the analysis of the lowest order term $\mathbb{E}\{\varphi_T^2\}$ is highly nontrivial), while the accuracy improvement is minor. Moreover, the cumulant expansion (30) was shown to have a finite radius of convergence, i.e., there is a maximal gradient, above which the cumulant expansion diverges [124, 125]. In other words, the inclusion of more terms would not improve the accuracy of the cumulant expansion. The non-perturbative analysis is necessary at high gradients (see Sec. 3.5). Note that the expansions (29) and (30) are not equivalent mathematically, although they are used interchangeably in practice. While the cumulant expansion (30) is known to have a finite radius of convergence, the Taylor expansion (29) is formally converging for any gradient³. However, the use of either of these expansions becomes impractical for large moments.

³Since the nuclei cannot diffuse too far, too large values of the phase φ_T are extremely improbable. In other words, the probability density $p(\varphi)$ of the phase φ_T decays very rapidly as $|\varphi| \rightarrow \infty$ (e.g., $p(\varphi) = (2\pi\sigma^2)^{-1/2} \exp(-\frac{\varphi^2}{2\sigma^2})$ for unrestricted diffusion, where $\sigma^2 = \mathbb{E}\{\varphi_T^2\} = 2Db$). As a consequence, the signal which appears as the Fourier transform of $p(\varphi)$, is analytic, while its Taylor expansion converges everywhere.

What is the geometric information that the GPA helps to bring? As discussed above, the GPA relates the ADC_0 to the position autocorrelation function whose shape-dependence is intricate. For bounded domains, the PAF can be formally expressed through Laplacian eigenfunctions from which the time dependence of ADC_0 can be deduced [5]. However, this dependence can be rather complicated, especially for multiscale domains. For instance, ADC_0 was shown to exhibit an intermediate plateau for a two-scale domain (e.g., a thin annulus in which the “radial” diffusion between two coaxial cylinders rapidly becomes restricted, while the “angular” diffusion still remains unrestricted for a long time) [89]. While theoretical results on ADC_0 are scarce for intermediate times, there are general statements about the short-time and long-time asymptotic limits discussed below.

3.2.2 Short-time asymptotics

When the size of obstacles is much larger than the diffusion length \sqrt{DT} , most nuclei do not encounter any boundary during their motion. In other words, the majority of nuclei exhibit unrestricted diffusion, as they do not feel obstacles at all. Only the nuclei which started within a surface layer of width \sqrt{DT} near the walls, are affected, and their motion is effectively slowed down. The volume fraction of these affected nuclei can be estimated as $\sqrt{DT}S/V$, where S is the surface area of the walls, and V is the total volume of the domain. Since the macroscopic signal is formed by both surface-affected and unaffected nuclei, one can show that

$$\frac{\text{ADC}_0}{D} \simeq 1 - c_0\sqrt{DT} \frac{S}{V} \left[1 - \underbrace{\sqrt{DT}(c_1\kappa/D + c_2\rho/D - c_3H)}_{\text{next-order correction}} + O(DT) \right], \quad (40)$$

where c_0, \dots, c_3 are explicit constants. In Eq. (40), we also wrote the next-order correction term which may include permeability κ , surface relaxation ρ , and mean curvature H of the surface [108, 109]. Measuring the ADC_0 from the macroscopic signal, one can access the surface-to-volume ratio S/V of the medium and, potentially, other characteristics such as κ , ρ , and H . In practice, an accurate estimation of the parameters in front of the linear-order term is limited by noise.

The short-time asymptotic behavior of the signal and the related behavior for the ADC were thoroughly investigated and implemented experimentally [15, 107–110, 112–117]. In particular, the shape-dependent constant c_0 can

in general be written as [5]

$$c_0 = \frac{4}{3\sqrt{\pi}} \frac{\prec (t_2 - t_1)^{3/2} \succ}{\prec (t_2 - t_1) \succ} \left(\frac{1}{S} \int_{\partial\Omega} d\mathbf{r} (\mathbf{e} \cdot \mathbf{n}_r)^2 \right), \quad (41)$$

where the temporal average $\prec \dots \succ$ incorporates the temporal profile $f(t)$. In the last factor, the squared scalar products between the gradient direction \mathbf{e} and the unit normal vector \mathbf{n}_r is integrated over the boundary $\partial\Omega$. For instance, this integral is equal to 1, 1/2 and 1/3 for an interval, a disk, and a sphere, respectively. For very narrow gradient pulses ($\delta \rightarrow 0$), the ratio of two temporal averages is equal to $1/\sqrt{2}$, from which one retrieves the result derived by Mitra *et al.* [107]:

$$\text{ADC}_0 \simeq D \left(1 - \frac{4}{3\sqrt{\pi}} \sqrt{D\Delta} \frac{S}{Vd} + \dots \right), \quad (42)$$

where d is the space dimension (typically $d = 3$). For the Hahn echo with $\delta = \Delta$, one recovers another expression from [126]:

$$\text{ADC}_0 \simeq D \left(1 - \frac{32(2\sqrt{2} - 1)}{105\sqrt{\pi}} \sqrt{D\Delta} \frac{S}{V} + \dots \right). \quad (43)$$

The use of the short-time asymptotics is limited to relatively large-scale obstacles. For instance, water molecules diffuse on average few microns during one millisecond, and the obstacles should thus be much larger to estimate the surface-to-volume ratio of the medium. For instance, this ratio was experimentally determined for glass sphere packs [109, 115], for erythrocytes [110], and for various rock samples [15].

3.2.3 Long-time asymptotics: isolated pores

In the opposite limit of long times, the asymptotic behavior is drastically different for isolated and connected pores.

For an isolated pore of size L , diffusing nuclei explore the pore space many times and therefore average out the magnetic field inhomogeneity. In this motional narrowing regime (also known as motional averaging regime), the acquired phase φ_T becomes nearly Gaussian, as first pointed out by Robertson and then by Neuman [127, 128]. The leading term of the second moment can be found explicitly, from which the GPA implies

$$S \simeq S_0 \exp \left(-\zeta_{-1} \frac{\gamma^2 g^2 L^4}{D} \int_0^T dt [f(t)]^2 \right) \quad (\sqrt{DT} \gg L), \quad (44)$$

where ζ_{-1} is the geometry-dependent coefficient (e.g., $\zeta_{-1} = 1/120$ for a slab of width L , $\zeta_{-1} = 7/96$ for a cylinder of radius L , $\zeta_{-1} = 8/175$ for a sphere of radius L , see [5] for details). While the quadratic dependence on the gradient is preserved (due to the GPA), the signal in the motional narrowing regime has a very different dependence on L and D , as compared to Eq. (16) for unrestricted diffusion: (i) the diffusion coefficient D appears in the denominator because faster diffusion enhances the averaging of the applied gradient; and (ii) the signal (44) strongly depends on the size L of the confining pore, while the signal for unrestricted diffusion does not involve any geometric size at all.

The comparison of Eqs. (36, 44) yields

$$\text{ADC}_0 \simeq \zeta_{-1} \frac{L^4}{D} \frac{\int_0^T dt [f(t)]^2}{\prec (t_1 - t_2) \succ}, \quad (45)$$

where the last factor accounts for the temporal profile $f(t)$. For instance, one gets

$$\text{ADC}_0 \simeq \zeta_{-1} \frac{2L^4}{D\delta(\Delta - \delta/3)} \quad (46)$$

for a Stejskal-Tanner sequence with rectangular pulses. As expected for an isolated pore, the nuclei explore the whole available space, their mean-square displacement saturates, while ADC_0 decreases as the time Δ increases. Computing the ADC from the macroscopic signal, one can estimate the size of the pore (up to a numerical prefactor ζ_{-1} which is *a priori* not known).

3.2.4 Long-time asymptotics: connected pores

For a medium composed of interconnected pores or a tissue formed by cells with permeable membrane, the long-time asymptotics is different. In fact, although the motion is hindered and slowed down by obstacles or walls, the nuclei can explore new regions without limitation. The ADC is therefore expected to reach an asymptotic level $\text{ADC}_0(\infty)$ as $\Delta \rightarrow \infty$. The ratio \mathcal{T} between the intrinsic diffusion coefficient D and the limiting one $\text{ADC}_0(\infty)$ is called the tortuosity and used to characterize how “tortuous” the porous media are [112, 115, 117, 129–131]. This notion came from the studies of transport phenomena in porous media, in which the tortuosity was originally estimated from electric conductivity measurements [132, 133]. In NMR, the measured tortuosity can vary from sample to sample, e.g., $\mathcal{T} \simeq 1.5$ for a sphere pack or $\mathcal{T} \simeq 3.4$ for a rock sample [130].

The long-time limit of ADC can be obtained by using periodic homogenization techniques, in which the voxel is assumed to be formed by numerous

periodic copies of a smaller but representative volume of a tissue [134]. When the permeability is small enough, the effective diffusion tensor $\mathbf{D}_{j,k}^m$ for each compartment Ω_m of the voxel can be found as [135, 136]

$$\mathbf{D}_{j,k}^m = \frac{D}{v_m} \int_{\Omega_m} d\mathbf{r} [\nabla W_j^m(\mathbf{r})]_k \quad (j, k = 1, 2, 3), \quad (47)$$

where v_m is the volume fraction of Ω_m , and the auxiliary functions $W_j^m(\mathbf{r})$ can be computed by solving the Laplace equation in Ω_m with the Neumann boundary condition on its boundary:

$$\begin{aligned} \nabla^2 W_j^m(\mathbf{r}) &= 0 & (\mathbf{r} \in \Omega_m, j = 1, 2, 3), \\ \frac{\partial W_j^m(\mathbf{r})}{\partial n} &= 0 & (\mathbf{r} \in \partial\Omega_m, j = 1, 2, 3). \end{aligned} \quad (48)$$

In addition, the pseudo-periodic boundary conditions are imposed at the outer boundary of the representative volume (see [135, 136] for details). We emphasize that the tensor \mathbf{D}^m is defined for any microstructure (under the assumption of its periodic extension) and is independent of gradient encoding. In practice, Eqs. (48) have to be solved numerically for a prescribed microstructure.

If the compartment Ω_m is bounded (e.g., the intracellular space englobed by a weakly permeable membrane), each solution $W_j^m(\mathbf{r})$ of Eq. (48) is constant, and Eq. (47) implies $\mathbf{D}^m = 0$, in agreement with Sec. 3.2.3. In turn, when the compartment Ω_m is connected to its periodic copies (e.g., the extracellular space), the effective diffusion tensor \mathbf{D}^m characterizes diffusion in the long-time limit. Diagonalizing this tensor, one can probe the macroscopic anisotropy of the voxel. When three eigenvalues of the tensor \mathbf{D}^m are equal, diffusion is macroscopically isotropic, and $\mathbf{D}^m = \text{ADC}_0(\infty)\mathbf{I}$, \mathbf{I} being the identity tensor. This homogenization approach yields the first-order approximation of the long-time ADC under the assumption of small permeability κ . The “smallness” can be claimed by comparing κ to D/L , L being an appropriate length scale. Alternative homogenization techniques can be used for highly permeable boundaries (e.g., see [137]).

The tortuosity reflects how the microstructure and surface exchange affect diffusion at long times. For instance, Crick proposed a simple relation between $\text{ADC}_0(\infty)$ and the permeability κ of equidistant barriers separated at distance a [138]

$$\frac{1}{\text{ADC}_0(\infty)} = \frac{1}{D} + \frac{1}{\kappa a}. \quad (49)$$

This relation was used by Tanner to estimate intercellular diffusion coefficients and membrane permeabilities for human red blood cells, adipose tissue,

and brine shrimp [21, 139] (see also [140, 141]). In spite of apparent limitations of this one-dimensional model (see discussion in [110]), the long-time behavior of the apparent diffusion coefficient can bring useful information about the medium.

The additional information about the medium can be gained by studying the asymptotic approach of ADC_0 to its limit as Δ increases. For a dilute suspension of reflecting spheres, de Swiet and Sen obtained [114]

$$\frac{\text{ADC}_0(\Delta)}{D} = \frac{1}{\mathcal{T}} + \frac{\beta_1}{\Delta} - \frac{\beta_2}{\Delta^{3/2}} + \dots \quad (\Delta \rightarrow \infty), \quad (50)$$

where β_1 and β_2 are constants that depend on microscopic details. The new leading term $\Delta^{-1/2}$ has to be added in the presence of permeable walls [116]. The two-point Padé approximation between the short-time asymptotics (42) and the long-time relation (50) was suggested to approximate the whole time-dependence of ADC_0 [109]. The asymptotic behavior (50) was believed to be universal [109, 114, 117, 142].

Recently, Novikov *et al.* have first questioned and then dispelled the universality of Eq. (50) for disordered media with permeable barriers [118, 119]. On one hand, the leading term $\Delta^{-1/2}$ was shown to remain universal for Brownian motion restricted by randomly placed and oriented permeable membranes (i.e., $(d-1)$ -dimensional planes in d dimensions), irrespective of the space dimension d . Its origin lies in the strong structural fluctuations introduced by the spatially extended random restrictions [118]. On the other hand, in a more general setting, the ADC was shown to approach the limiting value as

$$\frac{\text{ADC}_0(\Delta)}{D} \simeq \frac{1}{\mathcal{T}} + \frac{c}{\Delta^\theta} + \dots \quad (\Delta \rightarrow \infty), \quad (51)$$

where the dynamical exponent θ was related to the structural exponent p of the disorder as $\theta = (p+d)/2$ [119]. The structural exponent can be defined from the asymptotic behavior of the Fourier transform of the two-point structure correlation function: $\Gamma(k) \sim k^p$ as $k \rightarrow 0$. Structural universality classes of the medium can be distinguished by the exponent p : the ordered periodic arrangement ($p = \infty$), short-range disorder with a finite correlation length ($p = 0$), or strong disorder ($p < 0$) that can be achieved, e.g., by placing regular structural components (such as infinite lines, planes) with dimensionality $d_s < d$, in a random fashion, in which case $p = -d_s$. The above example of randomly placed $(d-1)$ -dimensional membranes corresponds to $p = -(d-1)$ and thus $\theta = 1/2$. The relation between the structural exponent p and the dynamical exponent θ allows one to determine from dMRI the most appropriate kind of model for mesoscopic structural disorder. In particular, Novikov *et al.* identified the relevant microscopic structure affecting

water diffusion measured with dMRI in muscles and in brain, and elucidated the corresponding microscopic changes providing clinically relevant dMRI contrast in ischemic stroke [119].

Strictly speaking, this study was focused on the mean-square displacement from which the $\text{ADC}_0(\Delta)$ could be deduced according to Eq. (35) under the narrow pulse approximation. An extension of the developed renormalization approach to more realistic gradient sequences is a promising perspective.

3.3 Diffusion in multi-compartmental tissue

Most dMRI experiments realized in biological tissues (such as brain or lungs) evidenced significant deviations from the mono-exponential behavior (28). As we discussed in Sec. 3.2.1, any attempt to interpret the conventional ADC defined as $-\ln(S(b)/S_0)/b$ does not make sense in this case. In turn, its extrapolated version, ADC_0 , is still meaningful and can bring useful information. However, the deviations from the mono-exponential behavior can be as well informative. For instance, the inclusion of the fourth-order term in Eq. (38) allows one to estimate the apparent diffusion kurtosis which was argued to be sensitive to tissue inhomogeneities [121, 122]. In general, a better understanding of the way how the tissue microstructure affects the measured signal over the whole available range of b -values, is necessary for a reliable interpretation of dMRI experiments. In this section, we discuss diffusion in multi-compartmental tissues and how such microstructure affects the macroscopic signal.

3.3.1 Multi-exponential and distributed signals

A biological tissue consists of cells which are separated from each other and from the extracellular space by semi-permeable membranes. This structural organization strongly affects water diffusion and the macroscopic signal. When the exchange between different compartments can be neglected, the total signal is a weighted linear combination of signals from compartments which, under the GPA (i.e., at weak gradients) reads as

$$\frac{S}{S_0} = \sum_j v_j \exp(-D_j b), \quad (52)$$

where v_j are the volume fractions of compartments (representing the relative amount of the nuclei), and D_j are their ADCs. Continuous analogs of the

multi-exponential signal are often called distributed models [143]:

$$\frac{S}{S_0} = \int_0^{\infty} dD' P(D') \exp(-D'b), \quad (53)$$

where $P(D')$ can be interpreted as the probability density (or relative fraction) of apparent diffusion coefficient D' . Note that Eq. (53) has a form of the Laplace transform of the density $P(D)$ with respect to the b -value. Inverting numerically Eqs. (52) or (53), one aims at recovering the distribution of ADCs (either D_j and their weights v_j , or the density $P(D')$). This distribution can in principle be related to the microstructure (see discussion in [144]). For instance, if the signal comes from many isolated pores, the ADC can be related to the size of the pore either in the long-time limit by Eq. (45), or in the short-time limit by Eqs. (42, 43). In the latter case, the characteristic size of a pore can be defined as $3V/S$. Numerous works focused on determining the pore size distribution (or length scales) of a sample from either diffusion-weighted signals or T_1/T_2 relaxation curves [43, 47, 130, 145–147]. However, the inversion of the Laplace transform is known to be an ill-posed problem, i.e., a small noise can drastically change inversion results [148]. Although many inversion techniques have been proposed (see [149, 150] and references therein), the inversion of the Laplace transform remains a difficult problem with unstable solutions. We emphasize that the distributed model (53) and the underlying density $P(D')$ can formally be introduced for any signal S which depends only on the b -value. While the b -value is still very broadly used as a combined proxy of gradient encoding, the signal typically exhibits more sophisticated dependence on the magnetic field parameters such as the gradient intensity, duration, and diffusion time. Further critical discussions of distributed or multiexponential models can be found in [151].

Note that the concept of distributed diffusivities allows one to produce numerous phenomenological models. For instance, choosing *a priori* the probability density $P(D)$ to be a Gamma distribution, $P(D) = D^{\nu-1}e^{-D/D_0}/(\Gamma(\nu)D_0^\nu)$ with two parameters ν and D_0 , the Laplace transform in Eq. (53) yields the power law dependence [152]

$$S = S_0(1 + bD_0)^{-\nu}. \quad (54)$$

This phenomenological expression can be used for fitting the experimental signal, while the fitted parameters D_0 and ν were argued as potential biomarkers of the biological tissue [153].

3.3.2 Bi-exponential model

If all cells or pores have similar shapes and sizes, their signals can be combined into an effective intracellular signal, yielding the famous bi-exponential form

$$\frac{S}{S_0} = v \exp(-D_i b) + (1 - v) \exp(-D_e b), \quad (55)$$

where v is the volume fraction of the (joint) intracellular compartment, and D_i and D_e are the apparent diffusion coefficients for both intra- and extracellular compartments. The bi-exponential form (55) has been employed in many biomedical applications, in particular, for brain dMRI [154–162]. For healthy brain region, the typical values of the bi-exponential form are: $D_i \simeq 0.25 \cdot 10^{-9} \text{ m}^2/\text{s}$, $D_e \simeq 1.4 \cdot 10^{-9} \text{ m}^2/\text{s}$, and $v \simeq 0.20 - 0.25$ [155]. Conventionally, the larger diffusion coefficient D_e is associated with faster hindered diffusion in the extracellular space, while the smaller diffusion coefficient D_i represents slower restricted diffusion in the intracellular compartments. Although the bi-exponential form (55) accurately fits the macroscopic signal in brain tissues, there is a strong mismatch between the values $v \sim 0.20 - 0.25$ estimated from the fit, and the values $v \sim 0.8$ from the histology of the same tissue [154]. In turn, numerous attempts to reconcile the mismatch and to amend the bi-exponential model did not yet resolve this problem (see [154–162] for further discussion). Nevertheless, the bi-exponential form is broadly applied for fitting experimental data.

Why does the bi-exponential form fail to capture the microstructure? In the first place, it is important to stress that an excellent fit of experimental data by a phenomenological curve does not prove that the underlying model is indeed applicable. In general, multi-exponential approximations are known as excellent fits for various decreasing functions [120, 163]. For instance, the function $S = 1/(1 + bD)$ can be well approximated by the bi-exponential form (55) over the conventional range $[0, 4000] \text{ s/mm}^2$ of b -values⁴. Two other examples of an excellent but strongly misleading approximation of the macroscopic signal by the bi-exponential fit were discussed in [75, 120]. Once experimental points are well fitted by Eq. (55), it is tempting to speculate why this is the right model. In turn, it is more challenging and time-consuming to explore the space of experimental parameters (e.g., to modify the diffusion time or the gradient pulse duration) and to identify those for which the bi-exponential fit does not work any more.

⁴For example, the bi-exponential form (55) with $D_i \simeq 0.33 \cdot 10^{-9} \text{ m}^2/\text{s}$, $D_e \simeq 2.83 \cdot 10^{-9} \text{ m}^2/\text{s}$, and $v \simeq 0.28$ accurately approximates the function $S = 1/(1 + bD)$ with $D = 3 \cdot 10^{-9} \text{ m}^2/\text{s}$, the maximal relative error being 6.6% over $0 \leq b \leq 4000 \text{ s/mm}^2$.

From theoretical point of view, there may be different reasons for the failure of the bi-exponential model. With no pretence for exhaustive analysis, we just recall that both D_e and D_i are apparent diffusion coefficients which are strongly affected by the microstructure and the gradient temporal profile [120]. For instance, since both D_i and D_e vary with time (e.g., in the long time limit, D_i vanishes, while D_e reaches a positive limit), measuring D_i and D_e on the same microstructure but at different diffusion times yields different values of the fraction v from the bi-exponential fit. This is illustrated in Fig. 4 which shows the macroscopic signal computed by a finite elements method (FEM) [46] for a periodic array of squares mimicking the intracellular space of volume fraction $v = 0.81$, while the connected outer region representing the extracellular space. Although this regular domain is not intended to model the complicated microstructure of the cerebral tissue, it allows us to illustrate some pitfalls of the phenomenological approach. Figure 4a shows the signals for seven inter-pulse times Δ ranging from 5 to 100 ms. In all cases, the bi-exponential formula (55) provides an excellent fit over the usual range of b -values from 0 to 4000 s/mm². The fit parameters as functions of Δ are shown in Fig. 4b. In particular, the volume fraction $1 - v$ of the extracellular space increases from 0.22 at $\Delta = 5$ ms to 0.44 at $\Delta = 100$ ms (the true geometric value being 0.19 by construction). This dependence on diffusion time is mainly caused by the exchange between the intra- and extracellular compartments. For comparison, the same parameters (shown by pluses, asterisks, and crosses) were obtained by fitting the macroscopic signals for impermeable boundary ($\kappa = 0$). In this case, the fitted parameters do not almost depend on Δ . Since the cellular membranes are permeable, the dependence of the parameters on the diffusion time can be a source of strongly misleading interpretations of dMRI signals in biological tissues.

3.3.3 Kärger model

In what follows, we focus on the role of exchange between the compartments which can significantly affect the signal. This exchange is characterized by the permeability κ of the cellular membrane which varies significantly among biological tissues (see Sec. 2.4). The permeation length D/κ typically exceeds cell sizes and diffusion lengths of dMRI experiment (Table 1). Roughly speaking, the membranes with κ below 10^{-6} m/s can be considered as (almost) impermeable, while the values of κ from 10^{-6} m/s to 10^{-4} m/s correspond to semi-permeable membranes (the “threshold” 10^{-6} m/s remaining qualitative).

Kärger *et al.* proposed a simple model to account for the exchange between compartments [164, 165]. The water molecules diffusing in the intra-

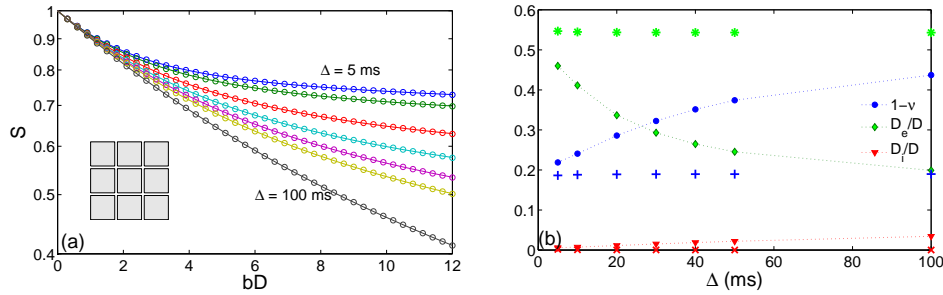


Figure 4: **(a)** Macroscopic signal computed by a FEM [46] for a periodic array of squares of size $L = 1.8 \mu\text{m}$, the neighboring centers being separated by distance $L_d = 2 \mu\text{m}$ (inset). The squares mimic the intracellular space of volume fraction $v = (L/L_d)^2 = 0.81$, while the connected outer region represents the extracellular space. The gradient direction is aligned with the horizontal axis. The water diffusion coefficient D and permeability κ are set to $3 \cdot 10^{-9} \text{ m}^2/\text{s}$ and 10^{-5} m/s , respectively. Seven solid lines show signals for different inter-pulse times: $\Delta = 5, 10, 20, 30, 40, 50, 100 \text{ ms}$, while the pulse duration was fixed at $\delta = 5 \text{ ms}$. The gradient range was adapted to keep the same maximal b -value fixed at 4000 s/mm^2 , as in many dMRI of brain tissue. Circles show the bi-exponential fit (55) to the signals. **(b)** The volume fraction $1 - v$ of the extracellular space and two ADCs, D_e/D and D_i/D , from the bi-exponential fit (55), versus Δ , are plotted by full symbols. For comparison, pluses, asterisks, and crosses show the same parameters fitted from the signals (not shown) computed on the same domain with impermeable boundary ($\kappa = 0$).

cellular and extracellular spaces were aggregated in two co-existing “pools” that both occupy the same volume of a voxel. The exchange between pools was assumed to be uncorrelated from diffusion and to follow the standard linear kinetics. In other words, the “belonging” of a molecule to one of two pools can switch randomly and independently of its motion. The concept of two effective pools is meant to replace the structural organization of the medium. The concentrations $c_1(\mathbf{r}, t)$ and $c_2(\mathbf{r}, t)$ of molecules in two pools obey the standard diffusion-reaction equations

$$\begin{aligned}\frac{\partial c_1(\mathbf{r}, t)}{\partial t} &= D_1 \nabla^2 c_1(\mathbf{r}, t) - \omega_{21} c_1(\mathbf{r}, t) + \omega_{12} c_2(\mathbf{r}, t), \\ \frac{\partial c_2(\mathbf{r}, t)}{\partial t} &= D_2 \nabla^2 c_2(\mathbf{r}, t) - \omega_{12} c_2(\mathbf{r}, t) + \omega_{21} c_1(\mathbf{r}, t),\end{aligned}\tag{56}$$

where the second and third terms in the right-hand side describe exchange between two pools, ω_{21} and ω_{12} being the exchange rates of moving from the first pool to the second pool, and vice-versa. These exchange rates can be related to the permeability κ and the surface-to-volume ratio S/V of the medium: $\omega_{21} = \kappa(S/V)/v_1$ and $\omega_{12} = \kappa(S/V)/v_2$, v_j being the volume fractions of two pools (with $v_1 + v_2 = 1$). Since the pools substitute the microstructure, these equations have no boundary conditions. Under the narrow pulse approximation, the signals in both compartments are obtained by taking the Fourier transform of these equations with respect to the wavevector $\mathbf{q} = \gamma \delta \mathbf{g}$. As a consequence, these signals satisfy two ordinary differential equations

$$\begin{aligned}\frac{dS_1(t)}{dt} &= -(D_1 |\mathbf{q}|^2 + \omega_{21}) S_1(t) + \omega_{12} S_2(t), \\ \frac{dS_2(t)}{dt} &= -(D_2 |\mathbf{q}|^2 + \omega_{12}) S_2(t) + \omega_{21} S_1(t),\end{aligned}\tag{57}$$

which are supplemented by the initial conditions $S_j(0) = v_j$. These equations are then solved analytically to get the explicit formula for the macroscopic signal (as the sum of these two contributions):

$$S = \nu \exp(-D_+ |\mathbf{q}|^2 \Delta) + (1 - \nu) \exp(-D_- |\mathbf{q}|^2 \Delta),\tag{58}$$

where $\nu = \frac{(v_1 D_1 + v_2 D_2) - D_-}{D_+ - D_-}$, and

$$\begin{aligned}D_{\pm} &= \frac{1}{2} \left((D_1 + D_2) + \frac{\omega_{12} + \omega_{21}}{|\mathbf{q}|^2} \right. \\ &\quad \left. \pm \sqrt{\left((D_2 - D_1) + \frac{\omega_{21} - \omega_{12}}{|\mathbf{q}|^2} \right)^2 + \frac{4\omega_{12}\omega_{21}}{|\mathbf{q}|^4}} \right).\end{aligned}\tag{59}$$

Fitting the macroscopic signal to Eq. (58), one can estimate both diffusion coefficients D_1 and D_2 , the volume fractions v_1 and v_2 , and the exchange rates ω_{12} and ω_{21} , from which the product $\kappa S/V$ can be deduced.

Although Eq. (58) resembles the bi-exponential form (55) by setting $b = |\mathbf{q}|^2 \Delta$, the effective diffusion coefficients D_{\pm} and the effective volume fraction ν depend on the gradient \mathbf{g} . Note also that the diffusion coefficients D_1 and D_2 in two pools should be different as otherwise there is no distinction between two pools, and Eq. (58) is simply reduced to Eq. (16) for unrestricted diffusion. An extension of the Kärger model to multiple compartments and to anisotropic diffusion is straightforward. Moreover, the Kärger model has been modified in various ways to produce a more accurate approximation of the PGSE signal and to describe restricted diffusion in bovine optic nerve [166], rat brain tissue [167, 168], suspension of erythrocytes [169–173], human breast cancer cells [174] and yeast cells [175].

The concept of co-existing effective pools has been justified by a coarse-graining argument [176]. To grasp the idea, one can imagine that the medium is virtually split into periodically arranged cubes whose size is (much) larger than the microstructural details (e.g., cells) but much smaller than the voxel size. Each cube would normally contain regions from both compartments. The coarse-grained concentrations $c_1(\mathbf{r}_c, t)$ and $c_2(\mathbf{r}_c, t)$ at the center \mathbf{r}_c of the cube are defined by averaging the local concentrations of water molecules in that region. In other words, the microstructure is coarse-grained to produce mesoscopic concentrations c_1 and c_2 . Although both c_1 and c_2 are now defined at discrete points (the centers of the cubes), the large number of these cubes allows one to replace discrete equations by their continuous analogs (56). This coarse-graining scheme is only applicable when the microscopic details are orders of magnitude smaller than the size of the voxel. In addition, the permeability should be small to justify the separation into two compartments and thus two pools [176].

An extension of the Kärger model beyond the NPA was proposed by Coatléven *et al.* [135, 136]. Using periodic homogenization techniques, the solution of the Bloch-Torrey equation was approximately reduced to the system of coupled differential equations for the relative signals S_j from the compartments Ω_j constituting the medium. For instance, when there are two compartments, Eqs. (57) are replaced by

$$\begin{aligned} \frac{dS_1(t)}{dt} &= -(D_1 \gamma^2 |\mathbf{g}|^2 c(t) + \omega_{21}) S_1(t) + \omega_{12} S_2(t), \\ \frac{dS_2(t)}{dt} &= -(D_2 \gamma^2 |\mathbf{g}|^2 c(t) + \omega_{12}) S_2(t) + \omega_{21} S_1(t), \end{aligned} \tag{60}$$

where $c(t) = \left(\int_0^t dt' f(t')\right)^2$. Under the NPA, one has $c(t) \simeq \delta^2$ and retrieves Eqs. (57). For non-narrow gradient pulses, the time dependence of $c(t)$ does not allow in general an analytical solution of Eqs. (60). In turn, a numerical solution of these ordinary differential equations is simpler and much faster than that of the Bloch-Torrey PDE (with space and time dependence). The effective diffusion coefficients D_1 and D_2 (or effective diffusion tensors for anisotropic diffusion) can in general be found by solving Eqs. (47, 48). The numerical solution of this Finite Pulse Kärger (FPK) model was confronted to the numerical solution of the Bloch-Torrey equation in several media such as mono- or polydisperse spheres/cylinders, Voronoi cells, etc. [136]. The FPK model accurately reproduces the macroscopic signal for non-narrow gradient pulses at moderate b -values (in a typical range between 0 and 4000 s/mm²). This model is applicable for small permeabilities (to prevent fast mixing of the nuclei between compartments), long diffusion times, and moderate gradients [135]. When the gradient pulses are not narrow, this model is more convenient for estimating the parameters than the original Kärger model [177].

3.3.4 Anomalous diffusion models

The probabilistic interpretation of the macroscopic signal as the characteristic function (5) of the random phase (4) can in principle accommodate any type of motion of the nuclei, including diffusive, convective, turbulent or even anomalous dynamics, the difference between various dynamics being hidden in the expectation \mathbb{E} . The generality of this approach opens numerous ways to extend the Bloch-Torrey equation. For instance, if the conventional Brownian motion is replaced by continuous time random walks (CTRW), the spatial and temporal derivatives in Eq. (3) can in general become fractional, incorporating nonlocal variations of the transverse magnetization in space and time [178–180]. These nonlocalities can mimic either long stalling periods in the motion of the nuclei, or their enhanced displacements. As a consequence, the macroscopic signal may inherit some anomalous features, e.g., the stretched-exponential dependence on inter-pulse time Δ and/or wavevector $\mathbf{q} = \gamma\delta\mathbf{g}$:

$$S \simeq S_0 \exp(-D_{\alpha,\beta} |\mathbf{q}|^{2\beta} \Delta^\alpha), \quad (61)$$

where α and β are two scaling exponents, and $D_{\alpha,\beta}$ is the generalized diffusion coefficient (in units m^{2 β} /s ^{α}) [181–186]. The standard Gaussian behavior is recovered at $\alpha = \beta = 1$. The stretched-exponential form (61) offered more degrees of freedom to fit the signal, while the fitted parameters (e.g., α and β) were suggested as potential biomarkers of biological tissues [187].

The major drawback of such anomalous diffusion models consists in lacking the microscopic ground. For instance, what is the origin of long stalling periods in the motion of the nuclei that might cause their subdiffusive behavior ($\alpha < 1$)? One may argue that the nuclei can remain restricted in small pores or confined in weakly permeable cells. In that case, the statistics of stalling times should be related to the pore size distribution and inter-pore exchange rates, or to variable permeabilities of cells. Whatever the expected mechanism of anomalous diffusion, it is important to relate the underlying phenomenological model and its microscopic origins, i.e., the microstructure of the tissue. This step is still missing in most phenomenological approaches.

3.3.5 Effective medium theory

A different approach to rationalize dMRI signals in heterogeneous media was proposed by Novikov and Kiselev [151]. They adopted the concept of effective medium theory (EMT), in which the microstructural details of a biological tissue, which are anyway inaccessible to dMRI, are treated as random “disorder”. The consequent statistical averaging allows one to substitute the original microscopically heterogeneous medium by an apparently homogeneous medium, whose observable macroscopic properties are modified by the microstructure. In this way, the geometric complexity of a biological tissue is captured through effective space-dependent parameters such as diffusion coefficient $D(\mathbf{r})$ or transverse relaxation $T_2(\mathbf{r})$. This coarse-graining is a statistical way to remove the boundary conditions of the Bloch-Torrey equation which implicitly determined the microstructure and presented the main challenges in its analysis. The statistical averaging, which is inherently present in the process of signal acquisition over a macroscopic voxel, is designed to make the macroscopic signals from both media as close as possible.

Under the NPA, the solution of the Bloch-Torrey equation in the effective medium can be related to the macroscopic signal. Assuming that stochastic fluctuations of the space-dependent diffusion coefficient are small, one can write the solution perturbatively as a formal infinite series and then average this series term-by-term over disorder realizations. The higher-order contributions are aggregated into the so-called self-energy part which quantifies how the complexity of the medium, on average, modifies the diffusive and relaxational Bloch-Torrey dynamics [151]. On one hand, the behavior of the self-energy can be related to the correlation functions of the disorder variation in space. On the other hand, the measurable relaxation and diffusion characteristics, such as the time-dependent diffusion coefficient and kurtosis, can be expressed through the self-energy. In this way, one relates the structural disorder and the macroscopic signal.

The general framework of EMT has numerous advantages aiming at identifying the most relevant geometric features that determine the macroscopic signal. As discussed in Sec. 3.2.4, this approach has been successfully applied to investigate the asymptotic behavior of the time-dependent diffusion coefficient [118, 119]. As the current limitations of the EMT, one can mention the assumption of (infinitely) narrow pulse gradients and the perturbative character which may prohibit using high gradients or considering strong disorder. Relaxing both limitations (e.g., by using renormalization techniques from quantum field theories) presents an interesting perspective. Elucidating the relation between the microstructure and the effective medium parameters is another promising direction.

3.4 Towards microscopic geometric models

Since the relation between the microstructure and the macroscopic signal is not yet fully understood, one often resorts to simplified models or fits. Typical examples are the kurtosis model (38), the distributed model (53), the bi-exponential model (55), the Kärger model (58), and the stretched-exponential model (61). These models accurately fit macroscopic signals over a moderate range of b -values, and their accuracy is often comparable (that can partly explain endless debates about the best choice among these models). As we already argued, the accuracy of the fit does not prove the validity of the model. In this light, the special attention should be paid to models which rely on the microstructure in the first place. We mention only one such model, the so-called cylinder model introduced by Callaghan [1]. This model starts from the signal in an isolated cylinder which under the GPA reads as

$$S_\alpha = S_0 \exp(-b[D_L \cos^2 \alpha + D_T \sin^2 \alpha]), \quad (62)$$

where D_L and D_T are the ADCs in the longitudinal and transverse directions, and α is the angle between the cylinder axis and the gradient direction. This separation is based on the independence of the displacements of the nuclei along the cylinder axis (longitudinal direction) and perpendicular to the cylinder axis (transverse direction). As a consequence, the dephasings in these directions are also independent while their characteristic functions are multiplied resulting in Eq. (62). If the medium is formed by randomly oriented identical cylinders, the macroscopic signal is obtained by averaging over orientations. For instance, if the cylinders are oriented uniformly in space, the average yields an explicit formula

$$S = S_0 \exp(-bD_T) \left(\frac{\pi}{4b(D_L - D_T)} \right)^{1/2} \operatorname{erf}([b(D_L - D_T)]^{1/2}), \quad (63)$$

where $\text{erf}(z)$ is the error function. Fitting the macroscopic signal to this explicit formula, one can determine both D_L and D_T , which, in turn, can be related to the length and the radius of the cylinder, according to Eq. (45). The cylinder model has been applied to interpret the measured ADCs in the lungs and in the brain, in which cylinders can approximate either alveolar ducts, or neurons [188–195]. This approximation obviously ignores many structural features, e.g., connectivity, internal structure, and bending of alveolar ducts, as well as permeation across neurons and presence of other compounds of the cerebral tissue. In spite of its simplistic character, the cylinder model allowed to diagnose some pathological changes in both organs. Many extensions of this model have been proposed, both for brain and lung dMRI (see [190, 194, 195] and references therein).

Other models accounting for the simplified geometric structure and some physiological features (such as permeation across membranes) were also developed e.g., arrays of spheres/cylinders [196, 197], composite hindered and restricted model of diffusion (CHARMED) [198], AxCaliber [199], etc. Some of these models rely on numerical simulations, the others propose approximate analytical formulas. An overview of 47 compartment models for analyzing dMRI signal in brain white matter, with a particular emphasis on limitations and pitfalls, is presented in [200]. We emphasize that modern numerical methods allow one to simulate the macroscopic signal in rather complicated microstructures and thus open new perspectives in interpretation of dMRI measurements [23, 46, 82].

3.5 Towards high gradients

Apparent diffusion coefficients, multi-exponential signals, and exchange models rely on the Gaussian phase approximation and are therefore limited to moderate gradients. Meanwhile, the current trend consists in increasing the diffusion-weighting gradients to make measurements more sensitive to the microstructure (e.g., the gradients as high as 380 mT/m and b -values up to 40000 s/mm² were employed to probe the geometric structure of the brain fiber pathways [10]). While modern dMRI scanners can produce high enough gradients to perform these experiments, there is no adequate theory to interpret them. Most interpretation attempts involved phenomenological models (e.g., multi-exponential, stretched-exponential, distributed, anomalous diffusion models) or numerical simulations. What do we know about the macroscopic signal at high gradients?

There are only several papers which dealt with this challenging problem. At high gradients, the macroscopic signal (16) for unrestricted diffusion is extremely small due to the strong dephasing of the nuclei. However, any prac-

tically relevant sample has a microstructure that would drastically change the signal at high gradients. Since the motion of the nuclei near obstacles or walls is more restricted, their transverse magnetization is less attenuated, as compared to the bulk magnetization. This effect, known as diffusive edge enhancement, has been observed experimentally [201] (see also [202]). So, what is the “residual” signal coming from the nuclei near the boundary? In the seminal paper, Stoller, Happer, and Dyson provided the first *non-perturbative* analysis of the one-dimensional Bloch-Torrey equation for the semi-axis with reflecting endpoint (which is equivalent to diffusion in the half-space when the gradient is applied perpendicular to the plane boundary) [74]. Ignoring the temporal profile (i.e., setting $f(t) = 1$), the Laplace transform reduces the Bloch-Torrey equation to the Airy equation:

$$\left(s + i\gamma gx - D \frac{\partial^2}{\partial x^2} \right) \mathcal{L}_s\{m(x, t)\} = m(x, 0), \quad (64)$$

where $\mathcal{L}_s\{m(x, t)\}$ is the Laplace-transformed magnetization, and $m(x, 0)$ is the initial condition. Changing the variable x to $w = s + i\gamma gx$ makes the relation to the Airy equation more explicit. Since a uniform density for the unbounded half-space (or semi-axis) is not appropriate, Stoller *et al.* considered a point-like source (located at x_0): $m(x, 0) = \delta(x - x_0)$. The resulting Laplace-transformed propagator can be found as a linear combination of Airy functions that satisfies the boundary condition $\frac{\partial}{\partial x} \mathcal{L}_s\{m(x, t)\} = 0$ at $x = 0$. Finally, inverting the Laplace transform by searching the poles of $\mathcal{L}_s\{m(x, t)\}$ and using the residue theorem allows one to return to the time domain

$$m(x, t; x_0) = \frac{1}{\ell_g} \sum_{n=1}^{\infty} \frac{e^{-\pi i/6}}{|a'_n| [\text{Ai}(a'_n)]^2} \exp(-e^{2\pi i/3} a'_n Dt/\ell_g^2) \text{Ai}(a'_n + ie^{-2\pi i/3} x/\ell_g) \text{Ai}(a'_n + ie^{-2\pi i/3} x_0/\ell_g), \quad (65)$$

where ℓ_g is the gradient length given by Eq. (15), $\text{Ai}(z)$ is the Airy function, and a'_n are the zeros of the derivative of the Airy function, $\text{Ai}'(a'_n) = 0$: $a'_1 \simeq -1.0188$, $a'_2 \simeq -3.2482$, etc. [74]. This exact expression allows one to further investigate the spatial behavior of the magnetization. In particular, the magnetization is shown to rapidly vanish when $x \gg \ell_g$. This effect is known as the localization of the magnetization near the barrier. Using Eq. (65), one can also deduce the macroscopic signal, for both free induction decay ($f(t) = 1$) and the pulsed-gradient spin-echo with two rectangular pulses (see [75, 126, 203] for details).

Figure 5a shows the magnetization $m(x, 2\Delta)$ at the echo time for restricted diffusion in a slab (between two parallel planes) under the rectangular

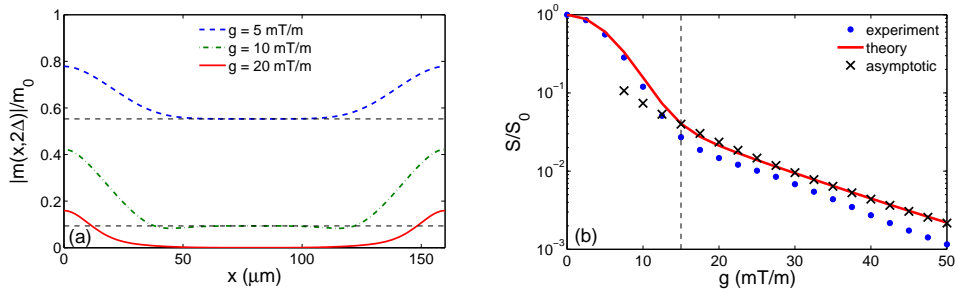


Figure 5: **(a)** Normalized absolute value of the transverse magnetization $m(x, 2\Delta)$ at the echo time 2Δ , for diffusion in a slab of width L , with $L = 160 \mu\text{m}$, $D = 2.3 \cdot 10^{-9} \text{ m}^2/\text{s}$, $\delta = \Delta = 60 \text{ ms}$, $m_0 = 1/L$, and three gradients: $g = 5, 10, 20 \text{ mT/m}$. At weak gradients, the signal is formed by the nuclei near the walls (less attenuated due to restriction) and the bulk nuclei (in the middle) whose normalized magnetization is given by the macroscopic signal for unrestricted diffusion e^{-Db} (horizontal dashed lines). At the gradient $g = 20 \text{ mT/m}$, the magnetization of the bulk nuclei is negligible, the only contribution coming from the nuclei near the walls. In this example, both the gradient length ($\ell_g \simeq 7.5 - 12.0 \mu\text{m}$) and the diffusion length ($\ell_D \simeq 16.6 \mu\text{m}$) are much smaller than L . However, the condition $\ell_g \ll \ell_D$ is not satisfied at weak gradients, and the GPA holds. **(b)** Macroscopic signal (solid line) versus the gradient g for the same problem. One can clearly see the transition from the Gaussian g^2 -behavior at weak gradients ($g \leq 15 \text{ mT/m}$) to the $g^{2/3}$ behavior in the localization regime at large gradients ($g \geq 15 \text{ mT/m}$) for which the asymptotic relation (67) is applicable (shown by crosses). The same transition is seen on the experimental curve (circles) reproduced from [204] (courtesy by M. D. Hürlimann).

temporal profile. We set $L = 160 \mu\text{m}$, $D = 2.3 \cdot 10^{-9} \text{ m}^2/\text{s}$, $\delta = \Delta = 60 \text{ ms}$, and three gradients $g = 5, 10, 20 \text{ mT/m}$ so that both the gradient length ($\ell_g \simeq 7.5 - 12.0 \mu\text{m}$) and the diffusion length ($\ell_D \simeq 16.6 \mu\text{m}$) are much smaller than L . Since the nuclei in the middle do not “feel” the presence of the walls, their dephasing is accurately described by the signal for unrestricted diffusion: $m(x, 2\Delta) \simeq m_0 e^{-Db}$. In turn, the nuclei near the walls are restricted and thus less attenuated. The resulting signal at weak gradients is therefore a combination of these two contributions. In turn, the magnetization becomes strongly attenuated in the middle at $g = 20 \text{ mT/m}$ so that only the nuclei near the boundary do contribute to the signal. This is a manifestation of the localization regime.

Remarkably, the presence of one reflecting barrier (endpoint) has dras-

tically changed the long-time asymptotic behavior of the macroscopic signal. For instance, for the Hahn echo ($\delta = \Delta$), the signal changes from $S = \exp(-2D\gamma^2 g^2 \delta^3/3)$ for unrestricted diffusion (no barrier) to [126]

$$S \propto \exp(-0.5|a'_1| D(2\delta)/\ell_g^2) = \exp(-|a'_1| (\gamma g)^{2/3} D^{1/3} \delta) \quad (66)$$

in the presence of a barrier. One can see that the time dependence has changed from δ^3 to δ and, most astonishingly, the conventional quadratic dependence on the gradient g has been replaced by the “anomalous” $g^{2/3}$ (or $b^{1/3}$) dependence. It seems that the dMRI community is so used to the quadratic dependence of the signal on g that the failure of the underlying Gaussian phase approximation at high gradients still remains difficult to accept. To our knowledge, the only experimental work by Hürlimann *et al.* has been undertaken to investigate this so-called localization regime [204]. In this experiment, the PGSE signal of water molecules was measured in a slab geometry of width $160 \mu\text{m}$. When the gradient was applied along the two parallel plates, the usual equation (16) for unrestricted diffusion was recovered. In turn, the signal attenuation in the perpendicular direction was shown to exhibit a transition from the GPA (28) at low gradients, to the $g^{2/3}$ dependence at high gradients, in agreement with Eq. (66). This behavior is illustrated on Fig. 5b, with both experimental signal (circles) reproduced from [204], and the numerical signal computed by a matrix formalism (solid line). Note that deviations between the theoretical and experimental curves can potentially be attributed to surface relaxation [5], nonrectangular temporal profile, small error in the angle between the gradient and the sample orientation, a gap between the sample and the sample holder, or residual mismatched eddy currents⁵. For instance, if the angle β between the gradient direction and the normal to the slab differs from zero (the expected perpendicular setting), the signal attenuation would also include the Gaussian factor from the lateral motion, i.e., $S(g \cos \beta) \exp(-Db \sin^2 \beta)$, where S is the signal attenuation in the transverse direction. At high gradients, even a small angle of 5° would significantly affect the experimental results.

For a slab domain, de Swiet and Sen provided more accurate asymptotic relation [126]

$$S \simeq 5.8841 \frac{L}{(\gamma g/D)^{1/3}} \exp(-|a'_1| (\gamma g)^{2/3} D^{1/3} \delta). \quad (67)$$

Figure 5b illustrates the excellent accuracy of this relation (shown by crosses).

⁵The author thanks Dr. M. Hürlimann for pointing out on some potential explanations of these deviations.

We emphasize that the transition between the GPA and the localization regime occurred at the rather moderate gradient $g_c \simeq 15$ mT/m. Nowadays, most clinical dMRI scanners can produce gradients 50 mT/m or higher, while scanners used in material sciences can go up to few T/m. In other words, the localization regime and the related signal decay are not exceptional “anomalies” under extreme experimental conditions. These features can be observed in ordinary experiments. Once the signal does not follow the classical mono-exponential decay in b -values, it is worth asking whether or not the localization regime may be responsible for this deviation. The reasoned answer to this question may avoid calling for phenomenological models when they are not necessary. We do not state that the localization regime is the only or even the major reason of observed deviations from the mono-exponential behavior. However, it should not be fully ignored either, as it is still a common practice nowadays.

In spite of the one-dimensional character of the above analysis, its results can be extended in several ways. Stoller *et al.* gave the non-perturbative solution for an interval with two reflecting endpoints [74]. de Swiet and Sen argued that the asymptotic behavior (66) is applicable in generic geometric restrictions [126]. More recently, the analysis of Stoller *et al.* has been extended to one-dimensional domains with semi-permeable barriers [75]. This extension allows one to investigate how the diffusive exchange between compartments influences the macroscopic signal at high gradients. In particular, the signal was shown to be more sensitive to the permeability at high gradients. Accounting for the inter-compartment exchange opens a new direction in understanding the localization mechanism itself. Tuning the permeability from 0 to infinity allows one to explore the transition in the signal behavior from impermeable to fully permeable barrier. In the limit $\kappa \rightarrow \infty$, the localization character progressively disappears and one retrieves Eq. (16) for unrestricted diffusion.

The gradient length ℓ_g determines the scales at which the localization regime becomes relevant. At long times when the diffusion length $\sqrt{D\Delta}$ greatly exceeds ℓ_g , the first term in Eq. (65) with $n = 1$ dominates over the other terms, resulting in the asymptotic decay (66). In other words, the localization regime emerges under the condition $\sqrt{D\Delta} \gg \ell_g$ (or $\Delta \gg \ell_g^2/D$). In addition, ℓ_g should be smaller than the geometric scales. Since the gradient length diverges as $g \rightarrow 0$, these conditions cannot be fulfilled at weak gradients, in which case the GPA applies. Although the weak dependence of ℓ_g on g does not allow one to significantly modify the gradient length, its typical range between 2 and 20 microns corresponds to length scales of many biological tissues and mineral porous media. As a consequence, the localization regime can be relevant for long dMRI sequences. We stress however

that further theoretical analysis is necessary for a better understanding of the localization regime and its applicability range in porous media.

We conclude this section by the rhetorical question: why has the localization regime been almost ignored so far by dMRI community? From theoretical point of view, the non-perturbative analysis of the Bloch-Torrey PDE and the related spectral theory of non-Hermitian operators are mathematically challenging [75, 205]. Even the one-dimensional case involves infinite series of complex-valued Airy functions whose asymptotic behavior is very sensitive to the phase of the argument. While Eq. (65) for the semi-axis with reflecting endpoint is fully explicit, its extensions to a semi-permeable barrier, an interval or an arrangement of intervals requires searching poles of combinations of Airy functions in the complex plane. The transition from the GPA to the localization regime is not well established (except for the case of an isolated interval, for which the localization regime is reduced to the motional narrowing regime, see [75]). Moreover, exact non-perturbative solutions in two and three dimensions are not known even for the simplest domains such as a disk or a sphere. From experimental point of view, the localization regime is often considered as “exotic” because in the gradient range, in which the asymptotic decay (66) is established, the macroscopic signal is rather attenuated. Generally, there is no clear experimental evidence that it is the localization regime which is responsible for deviations from the GPA (except for the work by Hürlimann *et al.* on the slab domain [204]). In spite of these remarks, a better understanding of signal formation at high gradients goes beyond a mere academic interest. While the asymptotic relation (66) may or may not be accurate in porous media, mastering the localization mechanism can help to reveal how the microstructure affects the macroscopic signal at high gradients and to design new dMRI protocols for more accurate inference of structural information on the sample (see further discussion in [75]).

4 Conclusions and perspectives

In this Chapter, we presented the mathematical background and several theoretical approaches to relate the microstructure to the macroscopic signal. Since the Bloch-Torrey equation implicitly incorporates the microstructure into the signal through boundary conditions, the inference of the geometric structure from the measured macroscopic signal remained challenging over the last sixty years. The current methodology relies on two successful approximations: the narrow pulse approximation and the Gaussian phase approximation. In the NPA, the specific temporal profile is chosen to reduce the Bloch-Torrey equation to diffusion equation, while the gradient encoding

re-appears through the Fourier transform. In the GPA, the gradient encoding is treated perturbatively at weak gradients, reducing again the problem to diffusion equation. Both approximations have been successfully applied to interpret experimental measurements and to infer geometric information. In spite of long-term intensive studies, numerous questions remain unanswered, while some known answers are incomplete or unsatisfactory. For instance, the macroscopic signals in multiscale porous media such as sedimentary rocks are still difficult to simulate while theoretical results remain scarce. The role of the inter-compartment exchange in biological tissues has got a considerable attention but the quantitative assessment of this influence requires further work. An adequate theory of signal formation at high gradients is still missing.

We deliberately focused on theoretical problems and progresses, but even with this restriction, the chapter could not include all the relevant results. For instance, we ignored numerous works on 2D and 3D correlation experiments, in which diffusion-weighting was combined with other weighting mechanisms such as T_1 and T_2 relaxation [206–211]. Many experimental advances will be discussed in the following chapters of this book.

Given the importance of reliable interpretations of dMRI signals, there are various opinions on the appropriate ways of further theoretical developments in this field. In particular, the choice of phenomenological versus microscopic geometric modeling is often debated. Moreover, the multitude of phenomenological models naturally provokes hot debates about which model is “the best” or “the true one”. While the first question can at least be answered in terms of the fit accuracy or the applicability range, the second question remains speculative. In general, phenomenological approaches are simpler and most suitable for getting “biomarkers” that would allow one to better distinguish different microscopic features of the tissue (e.g., lesions or tumors). Starting from basic ADC maps, one searches for the most robust and/or sensitive biomarkers. This is a well-defined practical goal of phenomenological models. At the same time, such approaches do not help to understand why the particular phenomenological model works better and under which circumstances it will fail. This is the primary purpose of microscopic geometric models. Since these models need *a priori* geometric assumptions and often rely on numerical computations, they are more difficult to operate with in practice. To some extent, these models aim at filling the gap between the microscopic mechanisms of signal formation and phenomenological models. The concept of disordered media and statistical averaging can be particularly valuable to deal with the geometric complexity of biological tissues. We believe that further progress in the field can be achieved by merging microscopic geometric models, statistical description of disordered

media, and high-gradient features of the signal formation. Such a joint theoretical approach can justify the use of some phenomenological fits and reveal new opportunities in dMRI.

References

- [1] P. T. Callaghan, *Principles of Nuclear Magnetic Resonance*, Microscopy, Clarendon Press, Oxford, 1991.
- [2] W. S. Price, *NMR Studies of translational Motion: Principles and Applications*, Cambridge University Press, 2009.
- [3] D. K. Jones, *Diffusion MRI: Theory, Methods, and Applications*, Oxford University Press, New York, USA, 2011.
- [4] P. T. Callaghan, *Translational Dynamics and Magnetic Resonance*, Oxford University Press, New York, USA, 2011.
- [5] D. S. Grebenkov, *NMR survey of reflected Brownian motion*, Rev. Mod. Phys., 2007, **79**, 1077-1137.
- [6] D. S. Tuch, T. G. Reese, M. R. Wiegell, and V. J. Wedeen, Diffusion MRI of Complex Neural Architecture, *Neuron* **40** (2003) 885-895.
- [7] J. Frahm, P. Dechent, J. Baudewig, and K. D. Merboldt, Advances in functional MRI of the human brain, *Prog. Nucl. Magn. Reson. Spectr.* **44** (2004) 1-32.
- [8] D. Le Bihan and H. Johansen-Berg, Diffusion MRI at 25: Exploring brain tissue structure and function, *NeuroImage* **61** (2012) 324-341.
- [9] H. C. Torrey, Bloch Equations with Diffusion Terms, *Phys. Rev.* **104** (1956) 563-565.
- [10] V. J. Wedeen, D. L. Rosene, R. Wang, G. Dai, F. Mortazavi, P. Hagmann, J. H. Kaas, and W.-Y. I. Tseng, The Geometric Structure of the Brain Fiber Pathways, *Science* **335**, 1628-1634 (2012).
- [11] M. Kac, On the distribution of certain Wiener functionals, *Trans. Am. Math. Soc.* **65**, 1-13 (1949).
- [12] M. Kac, On some connections between probability theory and differential and integral equations, in "Proc. 2nd Berkeley Symp. Math. Stat. Prob." edited by J. Neyman, pp. 189-215 (University of California Press, Berkeley, 1951).

- [13] M. Freidlin, *Functional Integration and Partial Differential Equations*, Annals of Mathematics Studies (Princeton University Press, Princeton, New Jersey, 1985).
- [14] P. P. Mitra and P. N. Sen, Effects of microgeometry and surface relaxation on NMR pulsed-field-gradient experiments: Simple pore geometries, *Phys. Rev. B* **45**, 143-156 (1992).
- [15] M. Hürlimann, K. G. Helmer, L. L. Latour, and C. H. Sotak, Restricted Diffusion in Sedimentary Rocks. Determination of Surface-Area-to-Volume Ratio and Surface Relaxivity, *J. Magn. Reson. A* **111**, 169-178 (1994).
- [16] A. Valfouskaya, P. M. Adler, J.-F. Thovert, and M. Fleury, Nuclear magnetic resonance diffusion with surface relaxation in porous media, *J. Coll. Int. Sci.* **295**, 188-201 (2006).
- [17] K. R. Brownstein and C. E. Tarr, Importance of Classical Diffusion in NMR Studies of Water in Biological Cells, *Phys. Rev. A* **19** (1979) 2446-2453.
- [18] A. V. Barzykin, K. Hayamizu, W. S. Price, and M. Tachiya, Pulsed-Field-Gradient NMR of Diffusive Transport through a Spherical Interface into an External Medium Containing a Relaxation Agent, *J. Magn. Reson. A* **114** (1995) 39-46.
- [19] W. S. Price, A. V. Barzykin, K Hayamizu, and M. Tachiya, A Model for Diffusive Transport through a Spherical Interface Probed by Pulsed-Field Gradient NMR, *Biophys. J.* **74** (1998) 2259-2271.
- [20] C. R. House, *Water Transport in Cells and Tissues*, Edward Arnold, Ltd., London, UK, 1974.
- [21] J. E. Tanner, Transient diffusion in a system partitioned by permeable barriers. Application to NMR measurements with a pulsed field gradient, *J. Chem. Phys.* **69**, 1748-1754 (1978).
- [22] P. W. Kuchel and C. J. Durrant, Permeability Coefficients from NMR q-Space Data: Models with Unevenly Spaced Semi-permeable Parallel Membranes, *J. Magn. Reson.* **139** (1999) 258-272.
- [23] D. S. Grebenkov, Pulsed-gradient spin-echo monitoring of restricted diffusion in multilayered structures, *J. Magn. Reson* **205**, 181-195 (2010).

- [24] E. L. Hahn Spin Echoes, *Phys. Rev.* **80**, 580-594 (1950).
- [25] H. Y. Carr and E. M. Purcell, Effects of diffusion on free precession in NMR experiments, *Phys. Rev.* **94**, 630-638 (1954).
- [26] S. Meiboom and D. Gill, Modified Spin-Echo Method for Measuring Nuclear Relaxation Times, *Rev. Sci. Instrum.* **29**, 688-691 (1958).
- [27] E. O. Stejskal, Use of Spin Echoes in a Pulsed Magnetic-Field Gradient to Study Anisotropic, Restricted Diffusion and Flow, *J. Chem. Phys.* **43**, 3597-3603 (1965).
- [28] J. E. Tanner and E. O. Stejskal, Restricted Self-Diffusion of Protons in Colloidal Systems by the Pulsed-Gradient, Spin-Echo Method, *J. Chem. Phys.* **49**, 1768-1777 (1968).
- [29] F. B. Laun, T. A. Kuder, W. Semmler, and B. Stieltjes, Determination of the Defining Boundary in Nuclear Magnetic Resonance Diffusion Experiments, *Phys. Rev. Lett.* **107**, 048102 (2011).
- [30] T. A. Kuder, P. Bachert, J. Windschuh, and F. B. Laun, Diffusion Pore Imaging by Hyperpolarized Xenon-129 Nuclear Magnetic Resonance, *Phys. Rev. Lett.* **111**, 028101 (2013).
- [31] S. Hertel, M. Hunter, and P. Galvosas, Magnetic resonance pore imaging, a tool for porous media research, *Phys. Rev. E* **87**, 030802 (2013).
- [32] E. C. Parsons, M. D. Does, and J. C. Gore, Temporal Diffusion Spectroscopy: Theory and Implementation in Restricted Systems Using Oscillating Gradients, *Magn. Reson. Med.* **55**, 75-84 (2006).
- [33] J. Xu, M. D. Does, and J. C. Gore, Quantitative characterization of tissue microstructure with temporal diffusion spectroscopy, *J. Magn. Reson.* **200**, 189-197 (2009).
- [34] D. S. Novikov and V. G. Kiselev, Surface-to-volume ratio with oscillating gradients, *J. Magn. Reson.* **210**, 141-145 (2011).
- [35] N. Shemesh, G. A. Alvarez, and L. Frydman, Measuring small compartment dimensions by probing diffusion dynamics via Non-uniform Oscillating-Gradient Spin-Echo (NOGSE) NMR, *J. Magn. Reson.* **237**, 49-62 (2013).
- [36] A. L. Sukstanskii, Exact analytical results for ADC with oscillating diffusion sensitizing gradients, *J. Magn. Reson.* **234**, 135-140 (2013).

- [37] P. P. Mitra, Multiple wave-vector extension of the NMR pulsed-field gradient spin-echo diffusion measurement, *Phys. Rev. B* **51**, 15074-15078 (1995).
- [38] Y. Cheng and D. G. Cory, Multiple scattering by NMR, *J. Am. Chem. Soc.* **121**, 7935-7936 (1999).
- [39] P. T. Callaghan and M. E. Komlosh, Locally anisotropic motion in a macroscopically isotropic system: displacement correlation measured using double pulsed gradient spin-echo NMR, *Magn. Reson. Chem.* **40**, S15-S19 (2002).
- [40] M. E. Komlosh, F. Horkay, R. Z. Freidlin, U. Nevo, Y. Assaf, and P. J. Basser, Detection of microscopic anisotropy in gray matter and in a novel tissue phantom using double Pulsed Gradient Spin Echo MR, *J. Magn. Reson.* **189**, 38-45 (2007).
- [41] E. Ozarslan, N. Shemesh, and P. J. Basser, A general framework to quantify the effect of restricted diffusion on the NMR signal with applications to double pulsed field gradient NMR experiments, *J. Chem. Phys.* **130**, 104702 (2009).
- [42] N. Shemesh, E. Ozarslan, P. J. Basser, and Y. Cohen, Detecting diffusion-diffraction patterns in size distribution phantoms using double-pulsed field gradient NMR: Theory and experiments, *J. Chem. Phys.* **132**, 034703 (2010).
- [43] D. Benjamini and U. Nevo, Estimation of pore size distribution using concentric double pulsed-field gradient NMR, *J. Magn. Reson.* **230**, 198-204 (2013).
- [44] S. Jespersen, Equivalence of double and single wave vector diffusion contrast at low diffusion weighting, *NMR Biomed.* **25**, 813-818 (2012).
- [45] J. Xu, M. D. Does, and J. C. Gore, Numerical study of water diffusion in biological tissues using an improved finite difference method, *Phys. Med. Biol.* **52**, N111-N126 (2007).
- [46] D. V. Nguyen, J.-R. Li, D. S. Grebenkov, and D. Le Bihan, An efficient finite-elements code to simulate diffusion MRI signals in complex tissue geometries, *J. Comput. Phys.* **263**, 283-302 (2014).
- [47] Y.-Q. Song, Using Internal Magnetic Fields to Obtain Pore Size Distribution of Porous Media, *Conc. Magn. Reson.* **18A**, 97-110 (2003).

- [48] D. S. Grebenkov, M. Filoche, and B. Sapoval, Spectral Properties of the Brownian Self-Transport Operator, *Eur. Phys. J. B* **36**, 221-231 (2003).
- [49] D. S. Grebenkov, Partially Reflected Brownian Motion: A Stochastic Approach to Transport Phenomena, in “Focus on Probability Theory”, Ed. L. R. Velle, pp. 135-169 (Nova Science Publishers, 2006).
- [50] D. S. Grebenkov, Analytical representations of the spread harmonic measure, *Phys. Rev. E* (submitted).
- [51] G. Wilemski and M. Fixman, General theory of diffusion-controlled reactions, *J. Chem. Phys.* **58**, 4009-4019 (1973).
- [52] H. Sano and M. Tachiya, Partially diffusion-controlled recombination, *J. Chem. Phys.* **71**, 1276-1282 (1979).
- [53] G. H. Weiss, Overview of theoretical models for reaction rates, *J. Stat. Phys.* **42**, 3-36 (1986).
- [54] B. Sapoval, General Formulation of Laplacian Transfer Across Irregular Surfaces, *Phys. Rev. Lett.* **73**, 3314-3316 (1994).
- [55] B. Sapoval, Transport Across Irregular Interfaces: Fractal Electrodes, Membranes and Catalysts, in “Fractals and Disordered Systems”, Eds. A. Bunde, S. Havlin (Springer, Berlin, 1996).
- [56] D. Holcman and Z. Schuss, Stochastic chemical reactions in microdomains, *J. Chem. Phys.* **122**, 114710 (2005).
- [57] D. S. Grebenkov, M. Filoche, and B. Sapoval, Mathematical Basis for a General Theory of Laplacian Transport towards Irregular Interfaces, *Phys. Rev. E* **73**, 021103 (2006).
- [58] A. Singer, Z. Schuss, A. Osipov, and D. Holcman, Partially Reflected Diffusion, *SIAM J. Appl. Math.* **68**, 844-868 (2008).
- [59] P. C. Bressloff, B. A. Earnshaw, and M. J. Ward, Diffusion of protein receptors on a cylindrical dendritic membrane with partially absorbing traps, *SIAM J. Appl. Math.* **68**, 1223-1246 (2008).
- [60] P. C. Bressloff and J. Newby, Stochastic models of intracellular transport, *Rev. Mod. Phys.* **85**, 135-196 (2013).

- [61] O. Bénichou and R. Voituriez, From first-passage times of random walks in confinement to geometry-controlled kinetics, *Phys. Rep.* **539**, 225-284 (2014).
- [62] P. J. McDonald, Stray field magnetic resonance imaging, *Progr. Nucl. Magn. Reson. Spectr.* **30**, 69-99 (1997).
- [63] D. A. T. Dick, The permeability coefficient of water in the cell membrane and the diffusion coefficient in the cell interior, *J. Theor. Biol.* **7**, 504-531 (1964).
- [64] J. D. Quirk, G. L. Bretthorst, T. Q. Duong, A. Z. Snyder, C. S. Springer, J. J. H. Ackerman, and J. J. Neil, Equilibrium water exchange between the intra- and extracellular spaces of mammalian brain, *Magn. Reson. Med.* **50**, 493-499 (2003).
- [65] H. Van As, Intact plant MRI for the study of cell water relations, membrane permeability, cell-to-cell and long-distance water transport, *J. Exper. Botany* **58**, 743-756 (2007).
- [66] D. S. Grebenkov, D. V. Nguyen, and J.-R. Li, Exploring diffusion across permeable barriers at high gradients. I. Narrow pulse approximation, *J. Magn. Reson.* **248**, 153-163 (2014).
- [67] W. Slijkerman, J. Hofman, Determination of surface relaxivity from NMR diffusion measurements, *Mag. Reson. Imag.* **16**, 541-544 (1998).
- [68] H. Liu, M. Nogueira d'Eurydice, S. Obruchkov, and P. Galvosas, Determining pore length scales and pore surface relaxivity of rock cores by internal magnetic fields modulation at 2 MHz NMR, *J. Magn. Reson.* **246**, 110-118 (2014).
- [69] R. L. Kleinberg, Utility of NMR T2 distributions, connection with capillary pressure, clay effect, and determination of the surface relaxivity parameter ρ_2 , *Magn. Reson. Imag.* **14**, 761-767 (1996).
- [70] V. M. Kenkre, E. Fukushima, and D. Sheltraw, Simple Solutions of the Torrey-Bloch Equations in the NMR Study of Molecular Diffusion, *J. Magn. Reson.* **128**, 62-69 (1997).
- [71] E. O. Stejskal and J. E. Tanner, Spin diffusion measurements: spin echoes in the presence of a time-dependent field gradient, *J. Chem. Phys.* **42** (1965), 288-292.

- [72] D. C. Douglass and D. W. McCall, Diffusion in Paraffin Hydrocarbons, *J. Phys. Chem.* **62**, 1102-1107 (1958).
- [73] D. E. Woessner, Self-Diffusion Measurements in Liquids by the Spin-Echo Technique, *Rev. Sci. Instr.* **31**, 1146 (1960).
- [74] S. D. Stoller, W. Happer, and F. J. Dyson, Transverse spin relaxation in inhomogeneous magnetic fields, *Phys. Rev. A* **44**, 7459-7477 (1991).
- [75] D. S. Grebenkov, Exploring diffusion across permeable barriers at high gradients. II. Localization regime, *J. Magn. Reson.* **248**, 164-176 (2014).
- [76] W. B. Hyslop and P. C. Lauterbur, Effects on restricted diffusion on microscopic NMR imaging, *J. Magn. Reson.* **94**, 501-510 (1991)
- [77] B. Balinov, B. Jönsson, P. Linse, and O. Söderman, The NMR Self-Diffusion Method Applied to Restricted Diffusion. Simulation of Echo Attenuation from Molecules in Spheres and Between Planes, *J. Magn. Reson. A* **104**, 17-25 (1993).
- [78] A. Coy and P. T. Callaghan, Pulsed Gradient Spin Echo nuclear magnetic resonance for molecules diffusing between partially reflecting rectangular barriers, *J. Chem. Phys.* **101**, 4599-4609 (1994).
- [79] A. Duh, A. Mohorič, and J. Stepišnik, Computer Simulation of the Spin-Echo Signal Distribution in the Case of Restricted Self-Diffusion, *J. Magn. Reson.* **148**, 257-266 (2001).
- [80] R. M. E. Valckenborg, H. P. Huinink, J. J. v. d. Sande, and K. Kopinga, Random-walk simulations of NMR dephasing effects due to uniform magnetic-field gradients in a pore, *Phys. Rev. E* **65**, 021306 (2002).
- [81] D. S. Grebenkov, G. Guillot, and B. Sapoval, Restricted Diffusion in a Model Acinar Labyrinth by NMR. Theoretical and Numerical Results, *J. Magn. Reson.* **184**, 143-156 (2007).
- [82] D. S. Grebenkov, A fast random walk algorithm for computing the pulsed-gradient spin-echo signal in multiscale porous media, *J. Magn. Reson.* **208**, 243-255 (2011).
- [83] R. C. Wayne and R. M. Cotts, Nuclear-magnetic resonance study of self-diffusion in a bounded medium, *Phys. Rev.* **151**, 264-272 (1966).

- [84] M. H. Blees, The effect of finite duration of gradient pulses on the pulsed-field-gradient NMR method for studying restricted diffusion, *J. Magn. Reson. A* **109**, 203-209 (1994).
- [85] P. N. Sen, A. André, and S. Axelrod, Spin echoes of nuclear magnetization diffusing in a constant magnetic field gradient and in a restricted geometry, *J. Chem. Phys.* **111**, 6548-6555 (1999).
- [86] S. N. Hwang, C. L. Chin, F. W. Wehrli, and D. B. Hackney, An image-based finite difference model for simulating restricted diffusion, *Magn. Reson. Med.* **50**, 373-382 (2003).
- [87] A. V. Barzykin, Exact solution of the Torrey-Bloch equation for a spin echo in restricted geometries, *Phys. Rev. B* **58**, 14171-14174 (1998) .
- [88] A. V. Barzykin, Theory of spin echo in restricted geometries under a step-wise gradient pulse sequence, *J. Magn. Reson.* **139**, 342-353 (1999).
- [89] D. S. Grebenkov, Analytical solution for restricted diffusion in circular and spherical layers under inhomogeneous magnetic fields, *J. Chem. Phys.* **128**, 134702 (2008).
- [90] D. S. Grebenkov, Laplacian Eigenfunctions in NMR I. A Numerical Tool, *Conc. Magn. Reson.* **32A**, 277-301 (2008).
- [91] D. S. Grebenkov, Laplacian eigenfunctions in NMR. II. Theoretical advances, *Conc. Magn. Reson.* **34A**, 264-296 (2009).
- [92] D. S. Grebenkov and B.-T. Nguyen, Geometrical structure of Laplacian eigenfunctions, *SIAM Rev.* **55**, 601-667 (2013).
- [93] A. Caprihan, L. Z. Wang, and E. Fukushima, A multiple-narrow-pulse approximation for restricted diffusion in a time-varying field gradient, *J. Magn. Reson. A* **118**, 94-102 (1996).
- [94] P. T. Callaghan, A simple matrix formalism for spin echo analysis of restricted diffusion under generalized gradient waveforms, *J. Magn. Reson.* **129**, 74-84 (1997).
- [95] A. L. Sukstanskii and D. A. Yablonskiy, Effects of Restricted Diffusion on MR Signal Formation, *J. Magn. Reson.* **157**, 92-105 (2002).
- [96] H. S. Carslaw and J. C. Jaeger, *Conduction of Heat in Solids*, 2nd Ed. (Clarendon, Oxford, 1959).

- [97] J. Crank, *The Mathematics of Diffusion*, 2nd Ed. (Clarendon, Oxford, 1975).
- [98] P. T. Callaghan, A. Coy, D. MacGowan, K. J. Packer, and F. O. Zelaya, Diffraction-Like Effects in NMR Diffusion Studies of Fluids in Porous Solids, *Nature* **351**, 467-469 (1991).
- [99] P. T. Callaghan, A. Coy, T. P. J. Halpin, D. MacGowan, K. J. Packer, and F. O. Zelaya, Diffusion in porous systems and the influence of pore morphology in pulsed gradient spin-echo nuclear magnetic resonance studies, *J. Chem. Phys.* **97**, 651-662 (1992).
- [100] P. T. Callaghan, Pulsed Gradient Spin Echo NMR for planar, cylindrical and spherical pores under conditions of wall relaxation, *J. Magn. Reson. A* **113**, 53-59 (1995).
- [101] D. Le Bihan and E. Breton, Imagerie de diffusion in-vivo par resonance magnetique nucleaire, *C. R. Acad. Sci. (Paris)* **301**, 1109-1112 (1985).
- [102] B. T. Saam, D. A. Yablonskiy, V. D. Kodibagkar, J. C. Leawoods, D. S. Gierada, J. D. Cooper, S. S. Lefrak, and M. S. Conradi, MR imaging of diffusion of ^3He gas in healthy and diseased lungs, *Magn. Reson. Med.* **44**, 174-179 (2000).
- [103] H. E. Moller, X. J. Chen, B. Saam, K. D. Hagspiel, G. A. Johnson, T. A. Altes, E. E. de Lange, and H.-U. Kauczor, MRI of the lungs using hyperpolarized noble gases, *Magn. Reson. Med.* **47**, 1029-1051 (2002).
- [104] E. J. R. van Beek, J. M. Wild, H.-U. Kauczor, W. Schreiber, J. P. Mugler, E. E. de Lange, Functional MRI of the Lung Using Hyperpolarized ^3He -Helium Gas, *J. Magn. Reson. Imaging* **20**, 540-554 (2004).
- [105] A. J. Swift, J. M. Wild, S. Fichelle, N. Woodhouse, S. Fleming, J. Waterhouse, R. A. Lawson, M. N. J. Paley, and E. J. R. van Beek, Emphysematous changes and normal variation in smokers and COPD patients using diffusion ^3He MRI, *Eur. J. Radiol.* **54**, 352-358 (2005).
- [106] S. B. Fain, S. R. Panth, M. D. Evans, A. L. Wentland, J. H. Holmes, F. R. Korosec, M. J. O'Brien, H. Fountaine, and T. M. Grist, Early Emphysematous Changes in Asymptomatic Smokers: Detection with ^3He MR Imaging, *Radiology* **239**, 875-883 (2006).
- [107] P. P. Mitra, P. N. Sen, L. M. Schwartz, and P. Le Doussal, Diffusion propagator as a probe of the structure of porous media, *Phys. Rev. Lett.* **68**, 3555-3558 (1992).

- [108] P. P. Mitra, P. N. Sen, and L. M. Schwartz, Short-time behavior of the diffusion coefficient as a geometrical probe of porous media, *Phys. Rev. B* **47**, 8565-8574 (1993).
- [109] L. L. Latour, P. P. Mitra, R. L. Kleinberg, and C. H. Sotak, Time-dependent diffusion coefficient of fluids in porous media as a probe of surface-to-volume ratio, *J. Magn. Reson. A* **101**, 342-346 (1993).
- [110] L. L. Latour, K. Svoboda, P. P. Mitra, and C. H. Sotak, Time-dependent diffusion of water in a biological model system, *Proc. Natl. Acad. Sci. U.S.A.* **91**, 1229-1233 (1994).
- [111] A. Szafer, J. Zhong, and J. C. Gore, Theoretical model for water diffusion in tissues, *Magn. Reson. Med.* **33**, 697-712 (1995).
- [112] K. G. Helmer, B. J. Dardzinski, and C. H. Sotak, The application of porous-media theory to the investigation of time-dependent diffusion in in vivo systems, *NMR Biomed.* **8**, 297-306 (1995).
- [113] K. G. Helmer, M. D. Hürlimann, T. M. de Swiet, P. N. Sen, and C. H. Sotak, Determination of ratio of surface area to pore volume from restricted diffusion in a constant field gradient, *J. Magn. Reson. A* **115**, 257-259 (1995).
- [114] T. M. de Swiet and P. N. Sen, Time dependent diffusion coefficient in a disordered medium, *J. Chem. Phys.* **104**, 206-209 (1996).
- [115] R. W. Mair, G. P. Wong, D. Hoffmann, M. D. Hrlimann, S. Patz, L. M. Schwartz, and R. L. Walsworth, Probing porous media with gas diffusion NMR, *Phys. Rev. Lett.* **83**, 3324-3327 (1999).
- [116] P. N. Sen, Time-dependent diffusion coefficient as a probe of permeability of the pore wall, *J. Chem. Phys.* **119**, 9871-9876 (2003).
- [117] P. N. Sen, Time-dependent diffusion coefficient as a probe of geometry, *Concepts Magn. Reson.* **23A**, 1-21 (2004).
- [118] D. S. Novikov, E. Fieremans, J. H. Jensen, and J. A. Helpert, Random walks with barriers, *Nat. Phys.* **7**, 508-514 (2011).
- [119] D. S. Novikov, J. H. Jensen, J. A. Helpert, and E. Fieremans, Revealing mesoscopic structural universality with diffusion, *Proc. Nat. Acad. Sci. USA* **111**, 5088-5093 (2014).

- [120] D. S. Grebenkov, Use, Misuse and Abuse of Apparent Diffusion Coefficients, *Conc. Magn. Reson. A* **36**, 24-35 (2010).
- [121] J. H. Jensen, J. A. Helpert, A. Ramani, H. Lu, and K. Kaczynski, Diffusional kurtosis imaging: the quantification of non-gaussian water diffusion by means of magnetic resonance imaging, *Magn. Reson. Med.* **53**, 1432-1440 (2005).
- [122] R. Trampel, J. H. Jensen, R. F. Lee, I. Kamenetskiy, G. McGuinness, and G. Johnson, Diffusional Kurtosis imaging in the lung using hyperpolarized ^3He , *Magn. Reson. Med.* **56**, 733-737 (2006).
- [123] D. S. Grebenkov, NMR Restricted Diffusion between Parallel Planes in a Cosine Magnetic Field: An Exactly Solvable Model, *J. Chem. Phys.* **126**, 104706 (2007).
- [124] A. F. Frøhlich, L. Østergaard, and V. G. Kiselev, Effect of Impermeable Boundaries on Diffusion-Attenuated MR Signal, *J. Magn. Reson.* **179**, 223-233 (2006).
- [125] V. G. Kiselev, The cumulant expansion: an overarching mathematical framework for understanding diffusion NMR, In *Diffusion MRI: Theory, Methods and Applications*, Jones DK (ed). Oxford University Press: Oxford, 2010; chapter 10.
- [126] T. M. de Swiet and P. N. Sen, Decay of nuclear magnetization by bounded diffusion in a constant field gradient, *J. Chem. Phys.* **100**, 5597-5604 (1994).
- [127] B. Robertson, Spin-echo decay of spins diffusion in a bounded region, *Phys. Rev.* **151**, 273-277 (1966).
- [128] C. H. Neuman, Spin echo of spins diffusion in a bounded medium, *J. Chem. Phys.* **60**, 4508-4511 (1974).
- [129] P. N. Sen, L. M. Schwartz, P. P. Mitra, and B. I. Halperin, Surface relaxation and the long-time diffusion coefficient in porous media: periodic geometries, *Phys. Rev. B* **49**, 215-225 (1994).
- [130] L. L. Latour, R. L. Kleinberg, P. P. Mitra, and C. H. Sotak, Pore-Size Distributions and Tortuosity in Heterogeneous Porous Media, *J. Magn. Reson. A* **112**, 83-91 (1995).

- [131] J. Pfeuffer, W. Dreher, E. Sykova, and D. Leibfritz, Water signal attenuation in diffusion-weighted H NMR experiments during cerebral ischemia: influence of intracellular restrictions, extracellular tortuosity, and exchange, *Magn. Reson. Imaging* **16**, 1023-1032 (1998).
- [132] J. van Brakel and P. M. Heertjes, Analysis of Diffusion in Macroporous Media in Terms of a Porosity, a Tortuosity and a Constrictivity Factor, *Int. J. Heat Mass Transfer* **17**, 1093-1103 (1974).
- [133] N. Epstein, On tortuosity and the tortuosity factor in flow and diffusion through porous media, *Chem. Engng. Sci.* **44**, 777-779 (1989).
- [134] A. Bensoussan, J.-L. Lions, G. Papanicolaou, Asymptotic analysis for periodic structures, *Studies in Mathematics and its Applications*, vol. 5, (North-Holland Publishing Co., Amsterdam, 1978).
- [135] J. Coatléven, H. Haddard, and J.-R. Li, A new macroscopic model including membrane exchange for diffusion MRI, *SIAM J. Appl. Math.* **74**, 516-546 (2014).
- [136] J.-R. Li, H. T. Nguyen, D. V. Nguyen, H. Haddar, J. Coatléven, and D. Le Bihan, Numerical study of a macroscopic finite pulse model of the diffusion MRI signal, *J. Magn. Reson.* **248**, 54-65 (2014).
- [137] H. Cheng and S. Torquato, Effective conductivity of periodic arrays of spheres with interfacial resistance, *Proc.: Math. Phys. Eng. Sci.* **453**, 145-161 (1997).
- [138] F. Crick, Diffusion in Embryogenesis, *Nature* **225**, 420-422 (1970).
- [139] J. E. Tanner, Intracellular diffusion of water, *Arch. Biochem. Biophys.* **224**, 416-428 (1983).
- [140] J. G. Powles, M. J. D. Mallett, G. Rickayzen, and W. A. B. Evans, Exact analytic solutions for diffusion impeded by an infinite array of partially permeable barriers, *Proc. R. Soc. London, Ser. A: Mathematical and Physical Sciences* **436**, 391-403 (1992).
- [141] A. L. Sukstanskii, D. A. Yablonskiy, and J. J. H. Ackerman, Effects of permeable boundaries on the diffusion-attenuated MR signal: insights from a one-dimensional model, *J. Magn. Reson.* **170**, 56-66 (2004).
- [142] J. W. Haus and K. W. Kehr, Diffusion in regular and disordered lattices, *Phys. Rep.* **150**, 263-406 (1987).

- [143] D. A. Yablonskiy, J. L. Bretthorst, and J. J. H. Ackerman, Statistical Model for Diffusion Attenuated MR Signal, *Magn. Reson. Med.* **50**, 664-669 (2003).
- [144] D. A. Yablonskiy and A. L. Sukstanskii, Theoretical models of the diffusion weighted MR signal, *NMR Biomed.* **23**, 661-681 (2010).
- [145] Y.-Q. Song, S. Ryu, and P. Sen, Determining multiple length scales in rocks, *Nature* **407**, 178-181 (2000).
- [146] G. J. W. Goudappel, J. P. M. van Duynhoven, and M. M. W. Mooren, Measurement of Oil Droplet Size Distributions in Food Oil/Water Emulsions by Time Domain Pulsed Field Gradient NMR, *J. Coll. Int. Sci.* **239**, 535-542 (2001).
- [147] G. S. Padhy, C. Lemaire, E. S. Amirtharaj, and M. A. Ioannidis, Pore size distribution in multiscale porous media as revealed by DDIF-NMR, mercury porosimetry and statistical image analysis, *Colloids Surf. A* **300**, 222-234 (2007).
- [148] C. L. Epstein and J. Schotland, The Bad Truth about Laplace's Transform, *SIAM Rev.* **50**, 504-520 (2008).
- [149] L. Venkataramanan, Y.-Q. Song, and M. D. Hürlimann, Solving Fredholm Integrals of the First Kind with Tensor Product Structure in 2 and 2.5 Dimensions, *IEEE Trans. Sign. Proc.* **50**, 1917-1926 (2002).
- [150] J. Abate and P. P. Valko, Multi-precision Laplace transform inversion, *Int. J. Num. Meth. Engng.* **60**, 979-993 (2004).
- [151] D. S. Novikov and V. G. Kiselev, Effective medium theory of a diffusion-weighted signal, *NMR Biomed.* **23**, 682-697 (2010).
- [152] M. Röding, D. Bernin, J. Jonasson, A. Särkkä, D. Topgaard, M. Rudemo, and M. Nydén, The gamma distribution model for pulsed-field gradient NMR studies of molecular-weight distributions of polymers, *J. Magn. Reson.* **222**, 105-111 (2012).
- [153] F. Grinberg, E. Farrher, L. Ciobanu, F. Geffroy, D. Le Bihan, and N. J. Shah, Non-Gaussian Diffusion Imaging for Enhanced Contrast of Brain Tissue Affected by Ischemic Stroke, *PLOS One* **9**, e89225 (2014).

- [154] T. Niendorf, R. M. Dijkhuizen, D. S. Norris, M. van Lookeren Campagne, and K. Nicolay, Biexponential diffusion attenuation in various states of brain tissue: implications for diffusion-weighted imaging. *Magn. Reson. Med.* **36** (1996) 847-857.
- [155] R. V. Mulkern, H. Gudbjartsson, C. F. Westin, H. P. Zengingonul, W. Gartner, C. R. Guttmann, et al. Multicomponent apparent diffusion coefficients in human brain. *NMR Biomed.* **12**, 51-62 (1999).
- [156] C. A. Clark and D. Le Bihan, Water diffusion compartmentation and anisotropy at high b values in the human brain, *Magn. Reson. Med.* **44**, 852-859 (2000).
- [157] C.-L. Chin, F. W. Wehrli, S. N. Hwang, M. Takahashi, and D. B. Hackney, Biexponential diffusion attenuation in the rat spinal cord: Computer simulations based on anatomic images of axonal architecture, *Magn. Reson. Med.* **47**, 455-460 (2002).
- [158] J. V. Sehy, J. J. H. Ackerman, and J. J. Neil, Evidence that both fast and slow water ADC components arise from intracellular space, *Magn. Reson. Med.* **48**, 765-770 (2002).
- [159] G. J. Stanisz, Diffusion MR in biological systems: tissue compartments and exchange, *Isr. J. Chem.* **43**, 33-44 (2003).
- [160] A. Schwarcz, P. Bogner, P. Meric, J. Correze, Z. Berente, J. Pal, F. Gallyas, T. Doczi, B. Gillet, and J. Beloeil, The existence of biexponential signal decay in magnetic resonance diffusion-weighted imaging appears to be independent of compartmentalization, *Magn. Reson. Med.* **51**, 278-285 (2004).
- [161] Z. Ababneh, H. Beloeil, C. B. Berde, G. Gambarota, S. E. Maier, and R. V. Mulkern, Biexponential parameterization of diffusion and T2 relaxation decay curves in a rat muscle edema model: decay curve components and water compartments, *Magn. Reson. Med.* **54**, 524-531 (2005).
- [162] V. G. Kiselev and K. A. Il'yasov, Is the "biexponential diffusion" bil-exponential? *Magn. Reson. Med.* **57**, 464-469 (2007).
- [163] G. Beylkin and L. Monzón, On approximation of functions by exponential sums, *Appl. Comput. Harmon. Anal.* **19**, 17-48 (2005).

- [164] J. Kärger, NMR self-diffusion studies in heterogeneous systems, *Adv. Colloid. Interfac.* **23**, 129-148 (1985).
- [165] J. Kärger, H. Pfeifer, and W. Heink, Principles and applications of self-diffusion measurements by nuclear magnetic resonance, In *Advances in Magnetic Resonance*, Vol. 12, Waugh JS (ed). Academic Press: San Diego, CA, 1988; 1-89.
- [166] G. J. Stanisz, A. Szafer, G. A. Wright, and R. M. Henkelman, An Analytical Model of Restricted Diffusion in Bovine Optic Nerve, *Magn. Reson. Med.* **37**, 103-111 (1997).
- [167] C. Meier, W. Dreher, and D. Leibfritz, Diffusion in compartmental systems. I. A comparison of an analytical model with simulations, *Magn. Reson. Med.* **50**, 500-509 (2003).
- [168] C. Meier, W. Dreher, and D. Leibfritz, Diffusion in compartmental systems. II. Diffusion-weighted measurements of rat brain tissue in vivo and postmortem at very large b-values, *Magn. Reson. Med.* **50**, 510-514 (2003).
- [169] T. Conlon and R. Outhred, Water diffusion permeability of erythrocytes using an NMR technique, *Biochim. Biophys. Acta* **288**, 354-361 (1972).
- [170] J. Andrasko, Water diffusion permeability of human erythrocytes studied by a pulsed gradient NMR technique, *Biochim. Biophys. Acta* **428**, 304-311 (1976).
- [171] M. D. Herbst and J. H. Goldstein, A review of water diffusion measurement by NMR in human red blood cells, *Am. J. Physiol. Cell. Physiol.* **256**, C1097-C1104 (1989).
- [172] A. R. Waldeck, P. W. Kuchel, A. J. Lennon, and B. E. Chapman, NMR diffusion measurements to characterise membrane transport and solute binding, *Prog. Nucl. Mag. Res. Spectr.* **30**, 39-68 (1997).
- [173] G. J. Stanisz, J. G. Li, G. A. Wright, and R. M. Henkelman, Water dynamics in human blood via combined measurements of T2 relaxation and diffusion in the presence of gadolinium, *Magn. Reson. Med.* **39**, 223-233 (1998).
- [174] Y. Roth, A. Ocherashvili, D. Daniels, J. Ruizcabello, S. Maier, A. Orenstein, and Y. Mardor, Quantification of water compartmentation

- in cell suspensions by diffusion-weighted and T2-weighted MRI, *Magn. Reson. Imaging* **26**, 88-102 (2008).
- [175] I. Åslund, A. Nowacka, M. Nilsson, and D. Topgaard, Filter-exchange PGSE NMR determination of cell membrane permeability, *J. Magn. Reson.* **200**, 291-295 (2009).
- [176] E. Fieremans, D. S. Novikov, J. H. Jensen, and J. A. Helpert, Monte Carlo study of a two-compartment exchange model of diffusion, *NMR Biomed.* **23**, 711-724 (2010).
- [177] H. T. Nguyen, D. S. Grebenkov, D. V. Nguyen, C. Poupon, D. Le Bihan, and J.-R. Li, Parameter estimation using macroscopic dMRI signal models, *Phys. Med. Biol.* **60**, 3389-3413 (2015).
- [178] J.-P. Bouchaud and A. Georges, Anomalous diffusion in disordered media: Statistical mechanisms, models and physical applications, *Phys. Rep.* **195**, 127-293 (1990).
- [179] R. Metzler and J. Klafter, The random walk's guide to anomalous diffusion: a fractional dynamics approach, *Phys. Rep.* **339**, 1-77 (2000).
- [180] M. F. Shlesinger, J. Klafter, and G. Zumofen, Above, below and beyond Brownian motion, *Am. J. Phys.* **67**, 1253-1259 (1999).
- [181] M. Peyron, G. K. Pierens, A. J. Lucas, L. D. Hall, and R. C. Stewart, The modified stretched-exponential model for characterization of NMR relaxation in porous media, *J. Magn. Reson. A* **118**, 214-220 (1996).
- [182] K. M. Bennett, K. M. Schmainda, R. Bennett, D. B. Rowe, H. Lu, and J. S. Hyde, Characterization of continuously distributed cortical water diffusion fates with a stretched-exponential model, *Magn. Reson. Med.* **50**, 727-734 (2003).
- [183] M. G. Hall and T. R. Barrick, From diffusion-weighted MRI to anomalous diffusion imaging, *Magn. Reson. Med.* **59**, 447-455 (2008).
- [184] R. L. Magin, O. Abdullah, D. Baleanu, and X. Joe Zhou, Anomalous diffusion expressed through fractional order differential operators in the Bloch-Torrey equation, *J. Magn. Reson.* **190**, 255-270 (2008).
- [185] Palombo, Gabrielli, De Santis, Cametti, Ruocco, Capuani, Spatio-temporal anomalous diffusion in heterogeneous media by nuclear magnetic resonance, *J. Chem. Phys.* **135**, 034504 (2011).

- [186] M. Palombo, A. Gabrielli, V. D. P. Servedio, G. Ruocco, and S. Capuani, Structural disorder and anomalous diffusion in random packing of spheres, *Scient. Rep.* **3**, 2631 (2013).
- [187] X. Joe Zhou, Q. Gao, O. Abdullah, and R. L. Magin, Studies of Anomalous Diffusion in the Human Brain Using Fractional Order Calculus, *Magn. Reson. Med.* **63**, 562-569 (2010).
- [188] D. A. Yablonskiy, A. L. Sukstanskii, J. C. Leawoods, D. S. Gierada, G. L. Bretthorst, S. S. Lefrak, J. D. Cooper, and M. S. Conradi, Quantitative in vivo Assessment of Lung Microstructure at the Alveolar Level with Hyperpolarized ^3He Diffusion MRI, *Proc. Nat. Acad. Sci. USA* **99**, 3111-3116 (2002).
- [189] R. E. Jacob, G. Laicher, and K. R. Minard 3D MRI of non-Gaussian ^3He gas diffusion in the rat lung, *J. Magn. Reson.* **188**, 357-366 (2007).
- [190] A. L. Sukstanskii, J. D. Quirk, and D. A. Yablonskiy, Probing lung microstructure with hyperpolarized ^3He gradient echo MRI, *NMR Biomed.* **27**, 1451-1460 (2014).
- [191] C. D. Kroenke, J. J. H. Ackerman, and D. A. Yablonskiy, On the nature of the NAA diffusion attenuated MR signal in the central nervous system, *Magn. Reson. Med.* **52**, 1052-1059 (2004).
- [192] Y. Assaf, R. Z. Freidlin, G. K. Rohde, and P. J. Basser, New modeling and experimental framework to characterize hindered and restricted water diffusion in brain white matter, *Magn. Reson. Med.* **52**, 965-978 (2004).
- [193] S. N. Jespersen, C. D. Kroenke, L. Østergaard, J. J. H. Ackerman, and D. A. Yablonskiy, Modeling dendrite density from magnetic resonance diffusion measurements, *NeuroImage* **34**, 1473-1486 (2007).
- [194] S. N. Jespersen, C. R. Bjarkam, J. R. Nyengaard, M. M. Chakravarty, B. Hansen, T. Vosegaard, L. Østergaard, D. A. Yablonskiy, N.C. Nielsen, and P. Vestergaard-Poulsen, Neurite density from magnetic resonance diffusion measurements at ultrahigh field: comparison with light microscopy and electron microscopy, *NeuroImage* **49**, 205-216 (2010).
- [195] D. V. Nguyen, J.-R. Li, D. S. Grebenkov, and D. Le Bihan, Numerical study of a cylinder model of the diffusion MRI signal for neuronal dendrite trees, *J. Magn. Reson.* **252**, 103-113 (2015).

- [196] J. C. Ford and D. B. Hackney, Numerical model for calculation of apparent diffusion coefficients (ADC) in permeable cylinders: comparison with measured ADC in spinal cord white matter, *Magn. Reson. Med.* **37**, 387-394 (1997).
- [197] P. N. Sen and P. J. Basser, Modeling diffusion in white matter in the brain: a composite porous medium, *Magn. Reson. Imaging* **23**, 215-220 (2005).
- [198] Y. Assaf and P. J. Basser, Composite hindered and restricted model of diffusion (CHARMED) MR imaging of the human brain, *NeuroImage* **27**, 48-58 (2005).
- [199] Y. Assaf, T. Blumenfeld-Katzir, Y. Yovel, and P. J. Basser, Axc caliber: a method for measuring axon diameter distribution from diffusion MRI, *Magn. Reson. Med.* **59**, 1347-1354 (2008).
- [200] E. Panagiotaki, T. Schneider, B. Siow, M. G. Hall, M. F. Lythgoe, and D. C. Alexander, Compartment models of the diffusion MR signal in brain white matter: A taxonomy and comparison, *NeuroImage* **59**, 2241-2254 (2012).
- [201] T. M. de Swiet, Diffusive edge enhancement in imaging, *J. Magn. Reson. B* **109**, 12-18 (1995).
- [202] P. T. Callaghan, A. Coy, L. C. Forde, and C. J. Rofe, Diffusive Relaxation and Edge Enhancement in NMR Microscopy, *J. Magn. Reson. A* **101**, 347-350 (1993).
- [203] S. Axelrod and P. N. Sen, Nuclear magnetic resonance spin echoes for restricted diffusion in an inhomogeneous field: Methods and asymptotic regimes, *J. Chem. Phys.* **114**, 6878-6895 (2001).
- [204] M. D. Hürlimann, K. G. Helmer, T. M. de Swiet, P. N. Sen, and C. H. Sotak, Spin Echoes in a Constant Gradient and in the Presence of Simple Restriction, *J. Magn. Reson. A* **113**, 260-264 (1995).
- [205] B. Helffer, *Spectral Theory and its Applications*, Vol. 139 of Cambridge studies in advanced mathematics, Cambridge University Press, Cambridge, 2013.
- [206] M. D. Hürlimann and L. Venkataramanan, Quantitative Measurement of Two-Dimensional Distribution Functions of Diffusion and Relaxation in Grossly Inhomogeneous Fields, *J. Magn. Reson.* **157**, 31-42 (2002).

- [207] Y.-Q. Song, L. Venkataramanan, M. D. Hürlimann, M. Flaum, P. Frulla, and C. Straley, T1-T2 Correlation Spectra Obtained Using a Fast Two-Dimensional Laplace Inversion, *J. Magn. Reson.* **154**, 261-268 (2002).
- [208] P. T. Callaghan and I. Furó, Diffusion-diffusion correlation and exchange as a signature for local order and dynamics, *J. Chem. Phys.* **120**, 4032-4038 (2004).
- [209] L. Monteilhet, J.-P. Korb, J. Mitchell, and P. J. McDonald, Observation of exchange of micropore water in cement pastes by two-dimensional T2-T2 nuclear magnetic resonance relaxometry, *Phys. Rev. E* **74**, 061404 (2006).
- [210] K. E. Washburn and P. T. Callaghan, Tracking Pore to Pore Exchange Using Relaxation Exchange Spectroscopy, *Phys. Rev. Lett.* **97**, 175502 (2006).
- [211] L. M. Burcaw, M. W. Hunter, and P. T. Callaghan, Propagator-resolved 2D exchange in porous media in the inhomogeneous magnetic field, *J. Magn. Reson.* **205**, 209-215 (2010).